4-21-2014

Application of an Alternating Minimization Algorithm to Experimental DIC Microscopy Data for the Quantitative Determination of Sample Optical Properties

Matthew Joseph Bledsoe

APPLICATION OF AN ALTERNATING MINIMIZATION ALGORITHM TO EXPERIMENTAL DIC MICROSCOPY DATA FOR THE QUANTITATIVE DETERMINATION OF SAMPLE OPTICAL PROPERTIES

by

Matthew Joseph Bledsoe

A Thesis

Submitted in Partial Fulfillment of the

Requirements for the Degree of

Master of Science

Major: Electrical and Computer Engineering

The University of Memphis

May, 2014

DEDICATION

To my wife, Jasmine.

ACKNOWLEDGEMENTS

I would like to acknowledge the following individuals for their contribution to this work: Dr. Chrysanthe Preza for her mentorship and guidance during my investigation of this algorithm and Dr. Sharon King for her assistance in setting up the experimental investigation of the liquid crystal bias cells. Additionally I would like to express gratitude to Dr. Eddie Jacobs and Dr. Aaron Robinson for serving on my committee and for the influence they have had on my education over the years. Finally, I would like to thank my fellow lab members, Sreya Ghosh, Nurmohammed Patwary, and Shohag Hossain, for their support and encouragement.

ABSTRACT

Bledsoe, Matthew Joseph. MS. The University of Memphis. May 2014. Application of an Alternating Minimization Algorithm to Experimental DIC Microscopy Data for the Quantitative Determination of Sample Optical Properties. Major Professor: Dr. Chrysanthe Preza.

Differential Interference Contrast (DIC) is commonly chosen for imaging unstained transparent samples. One limitation of DIC microscopy is the qualitative results it provides. This must be post-processed to extract meaningful information. The Alternating Minimization (AM) algorithm studied in this thesis is an iterative approach to recover a quantitative estimate of a sample's complex-valued transmittance function. The AM algorithm is validated using simulated data. Additionally, the bias retardation and shear distance, two characteristic features of the DIC system, must be measured to insure the system model is accurate. This is accomplished by introducing a calibrated liquid crystal device to the system. Algorithm performance is verified using an experimental test object before finally being applied to biological samples. Overall results demonstrate the accuracy of this algorithm's object estimation results. These are verified through comparison to similar data processing techniques.

TABLE OF CONTENTS

LIST OF FIGURES

Figure Page

CHAPTER 1

INTRODUCTION

There are a wide range of microscopy modalities utilized in the scientific community. The selection of a specific modality is heavily predicated by the object or material being imaged and the desired information to be obtained during the imaging process. When performing biological research, there are many factors to consider in choosing how to image a given sample. Fluorescence techniques are useful when imaging thin samples with weak absorption properties; however the introduction of dyes and markers can be detrimental to the functioning of the sample. In these situations phase imaging techniques are useful as they do not require strong illumination sources or dyes to be utilized. Differential Interference Contrast (DIC) microscopy is one modality that produces an image of a sample's phase. DIC creates this phase image by utilizing interference imaging techniques to create a contrast image. The specifics of this modality are discussed in greater depth in Section 2.

1.1 Computational Imaging for Quantitative Phase Imaging

Phase imaging techniques produce qualitative representations of the underlying object being imaged. They can provide details about the general structure and composition of the sample, but this only allows inference of the true nature of the sample. DIC imaging in particular suffers from two major shortcomings: it is an amplitude encoding of the output of a complex-valued system and this encoding represents a unidirectional gradient of the object being imaged resulting in information loss for any detail that resides along that direction. As a result, significant post-processing is required to reach a quantitative representation of the sample to determine its true phase properties.

Many techniques have been investigated to recover this phase information. Those discussed in this thesis are spiral phase integration (SPI),[1, 2] rotational diversity (RD-DIC),[3] and an approach based on an alternating minimization algorithm (AMA).[4-8] These are discussed in more detail in Section 2.

The principle goal of computational imaging research is to create and refine mathematical models that represent an imaging system. There are many models required to fully simulate a given system as shown in Figure 1. Every aspect of the process, from the object being viewed to the optical properties of the microscope, must be given a mathematical representation. These are all tied together into one algorithm representative of the overall functioning of the hardware. This model must be verified by collecting experimental data and comparing it to simulated data generated by the algorithm. Any discrepancies must be resolved, the model updated, and new results created for further refinement. Once an acceptable model is created it can be used to assist in research for improvements to the system itself. This can either take the form of developing algorithms to post-process experimental data to correct for some defect or aberration present in the raw data or to simulate adjustments and additions of hardware to alleviate those issues before the data is gathered.

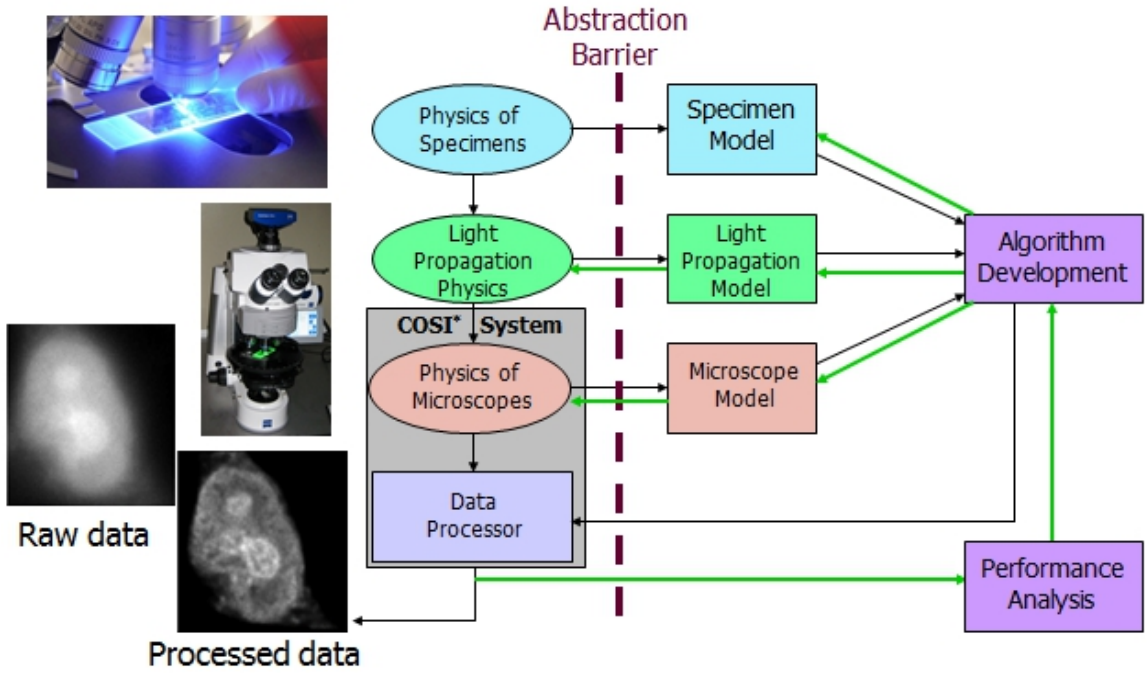

Figure 1. Flowchart detailing the development of system models in computational imaging and the relationship between experimental and simulated data collection. Figure courtesy of Dr. Preza.

Other groups are conducting quantitative phase imaging based on DIC microscopy for a wide variety of applications. Arnison and King developed a quantitative phase imaging technique called the Spiral Phase Integration (SPI) method utilizing phase shifting, rotational diversity, and a Fourier domain integration to recover a linear isotropic phase mask.[1, 2] While this approach does correct for the non-linearity issue in DIC imaging, it does not recover the magnitude portion of the complex-valued object function and also, it is based on simplified imaging model. The method in this thesis uses a full diffraction effect model. Using an expanded version of the imaging models utilized for this thesis, Sierra et al. have conducted work on recovering phase data

from 3-D DIC image sets.[9-12] Additionally, through the use of optical quadrature microscopy to create a morphological map of the sample, Sierra was able to create a refractive index map of the sample for a specific application, demonstrating the benefit of quantitative phase information. This approach utilizes DIC to only to find information on object morphology and moves the quantitative object estimation to another modality. Another body of research by Shribak et al., which contributed to the development of an orientation independent DIC implementation, is focused on recovering phase information for the sample as well as an understanding of the sample anisotropic, or birefringent, properties.[13-15] While similar in its utilization of multiple shear directions for reconstruction, this application focuses on analyzing birefringent samples to determine their anisotropic structures.

1.2 Alternating Minimization Algorithm

Recovery of a sample's phase information from a DIC image faces many challenges. The largest obstacle lies in the amplitude encoding of a complex system response. This results in an ill-posed inverse system with intractably many solutions. The RD-DIC algorithm handles this situation by assuming the specimen to be transparent and thus fully transmissive. This results in a relaxed problem that only involves estimating the objects phase. This AM algorithm extends the use of rotationally diverse datasets from semi-transparent objects by allowing the estimation of both magnitude and phase. The key tenant of the approach is a variational extension of the minimization objective function to include the complex valued object function as well as an additional

term representing the unrecorded phase of the measured data. This approach is well known and has applications in other forms of imaging research[16, 17] and other fields of research such as machine learning[18, 19] and statistics.[20]

1.3 Contribution of This Thesis to the AM Algorithm

Early publications on the AM algorithm covered the development of the algorithm itself and its application to simulated data. They covered the use of both noiseless and noisy simulations, a regularization function to mitigate the effects of noise, and the computation of various parameters necessary to the algorithm itself. Additionally, some initial work was done to apply the AM algorithm to experimental data of a yeast cell. This thesis continues the work completed for the above mentioned efforts. Some replication of previous results was conducted to ensure proper understanding of the algorithm and the optical system it is intended to simulate. The main objective is improvement of the algorithm's performance when applied to experimentally gathered data.

A large contribution to achieving this outcome is the introduction of a calibrated liquid crystal bias cell. This cell is used to introduce a known amount of phase bias to the DIC imaging system. It can also be used to accurately measure the shear distance created by the Nomarski prism which is used to create the DIC system. Additional work was done to improve the implementation of various portions of the simulation. Areas of work included the DIC point spread function (PSF) model implementation, AMA-specific parameter computations, registration of experimentally collected data, and some minor optimizations to improve computation times when working with larger datasets.

1.4 Thesis Organization

This thesis is broken down in four main portions. Some discussion of DIC microscopy in general is provided in Section 2. This chapter also contains a brief introduction to the SPI algorithm along with an introduction to the RD-DIC algorithm and its extension to the AM algorithm. Section 3 covers DIC PSF computations, the selection of simulated datasets, and executing the algorithm on these simulated datasets. Some previous investigations are also repeated to help validate new parameter selection equations. Section 4 explains calibration of the liquid crystal bias cell, using this calibration to determine the shear distance of the system, and using both of these advancements to improve the application of AMA to experimental datasets. New experimental data of a polystyrene bead is collected and analyzed and compared to simulated reproductions. The previously collected yeast data is also re-examined and these results are compared to the output of the SPI algorithm. Section 5 contains a summary of all work performed, some conclusions drawn, and Section 6 discusses future work to be done with this AM algorithm.

CHAPTER 2

BACKGROUND

2.1 DIC Image Formation

DIC microscopy is an optical illumination modality used to enhance contrast in unstained, transmissive samples. It works by using principles of interferometry to encode the difference in optical path length (OPL) of a sample. This is achieved through the use of coherent pairs of orthogonally polarized light separated by a known and consistent spacing. These pairs of light waves interact with portion of the sample separated by a small distance, called the shear distance, which is generally slightly below the sampling resolution of the objective lens being utilized to form the image. These two waves experience differing levels of phase shifting due to a combination of variations of thickness and refractive index across the sample. When recombined into a single light wave this shift serves to introduce constructive and destructive interference which gives rise to variations in intensity at the imaging plane and yields a qualitative representation of the phase gradient of the object along the axis of shear. A diagram of this system is shown in Figure 2.

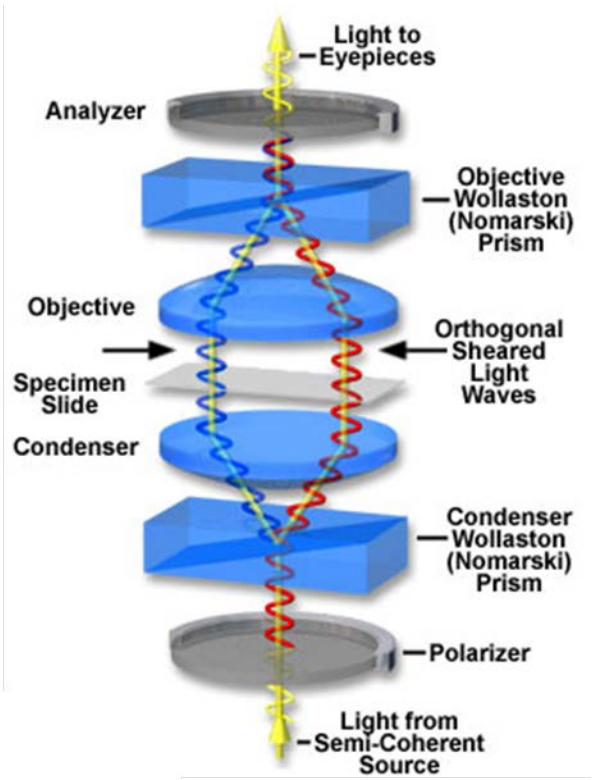

Figure 2. Diagram of microscope system setup for Nomarski DIC imaging. Light is polarized by the bottom filter at 45 degrees. The condenser Nomarski prism shears this light into two coherent waves of equal intensity polarized at 0 degrees and 90 degrees. These waves pass through adjacent portions of the specimen and each experiences a different OPL. The objective focuses the waves into the objective Nomarski prism which recombines each wave pair back into a single wave polarized at 135 degrees. Due to the variation in OPL each wave experienced they have different phase components which causes interference and leads to a change in intensity. This intensity variation is captured by the sensor and results in a contrast image of the object being viewed. Image courtesy of Olympus Microscopy.

Unpolarized light is introduced to the system and passed through a polarization filter before reaching the condenser side Nomarski prism. This polarization is introduced in such a way that the vibration direction is 45 degrees off from the optical axis of the first wedge in the condenser Nomarski prism and 90 degrees off from the vibration direction of the analyzer filter. This orientation is important. Polarizing the light at 45 degrees relative to the optical axis of the first wedge of the Nomarski prism causes it to be split into two coherent waves of equal intensity, orthogonal polarizations, and separated by a small lateral distance. The condenser lens directs the light onto the sample. The orthogonal polarization allows each plane wave to only be influenced by the optical properties of the sample itself, no interference occurs between the two.[21]

After passing through the sample, the light is focused by the objective lens into the analyzer side Nomarski prism. Again, the optical axis of this prism is aligned in such a way that the two plane waves strike at 45 degree offsets. Where the condenser prism split them into two equivalent orthogonal wave fronts, the analyzer prism recombines them into a single wave front. The lateral distance between each coherent wave pair results in two waves that passed through different portions of the specimen to be recombined into a single wave. Any difference in phase between the two components results in interference which is manifested as increased or decreased intensity of the image. The final result is an encoding of variations of OPL across the specimen along the direction of shear. One simplification of this model is to consider it as a superposition of two laterally shifted bright field images with differing phase components which results in an interference image when they are recombined.

The crucial component of this system is the use of Nomarski prisms, a modified version of Wollaston prisms. Both prisms are made by cementing together two wedges of a birefringent material as shown in Figure 3. In a Wollaston prism these two wedges have perpendicular optical axes which give rise to its shearing abilities. The key difference in Nomarski's approach was altering the way in which the second wedge is cut and attached. Rather than utilizing perpendicular optical axes, one of the wedges is cut so that its optical axis is oblique to the face of the prism. Selection of this angle allows for the interference plane of the sheared light waves to be focused outside of the prism. This allows it to be placed inside the focal plane of the objective lens.

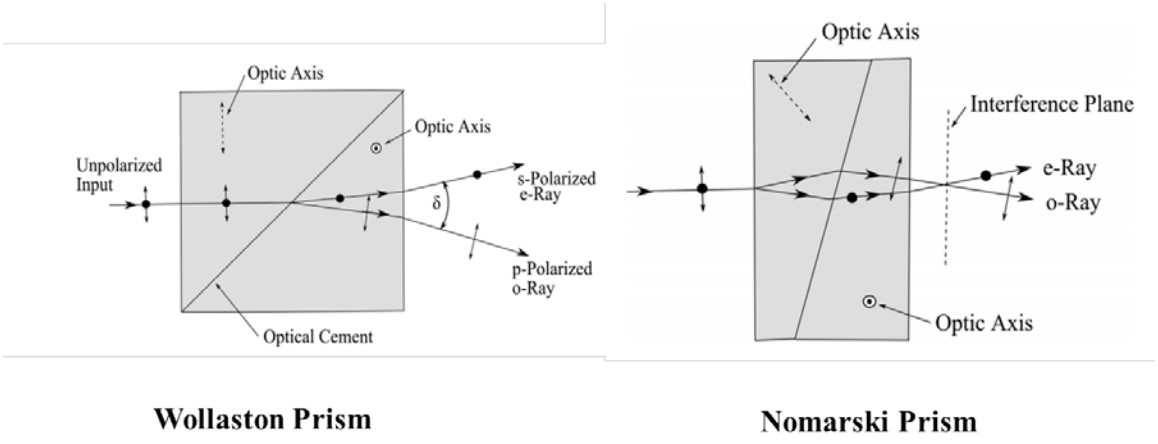

Figure 3. Comparison of the light shearing properties of Wollaston and Nomarski prisms. Both prisms introduce shear through their birefringent properties, however the Nomarski prism uses an oblique optical axis to allow focusing of these beams at a point on a plane external to the prism itself.

2.2 DIC PSF Model

The DIC PSF model utilized is an extension of previous work by Cogswell and Sheppard[22] to utilize theory proposed by Born and Wolf[23] regarding image formation

under partially coherent illumination. This work was completed by Preza, Snyder, and Conchello.[24] Image formation is the result of combining two phase shifted intensity images as outlined in Section 2.1. This phase shift can also be influenced by the intentional introduction of a known amount of a uniform phase shift, known as the bias retardation, to one of the two orthogonally polarized wave fronts. The complex amplitude difference in these waves can be given by

$$h(x,y) = (1-R)e^{-j\Delta\theta}k(x-\Delta x,y) - Re^{-j\Delta\theta}k(x+\Delta x,y), \quad (1)$$

where $2\Delta\theta$ is the bias retardation in radians, $2\Delta x$ is the shear distance in length (typically μm), $k(x, y)$ is the amplitude PSF from transmissive optics, and R is the amplitude ratio of the two polarized wavefronts.[3] An example PSF is shown in Figure 4.

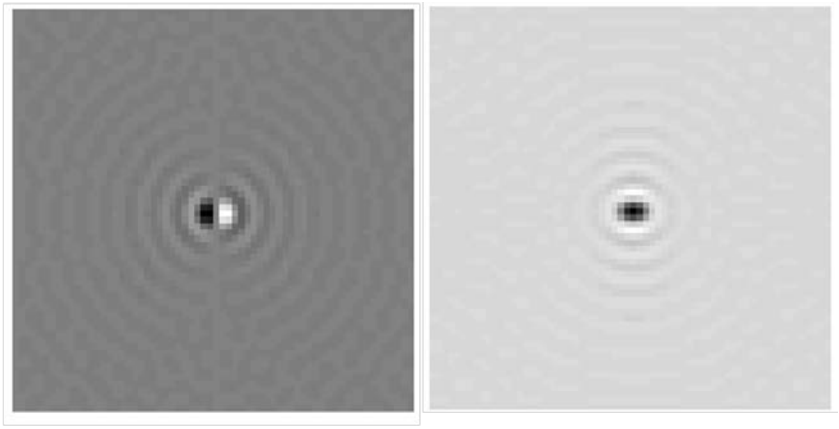

Figure 4. Images of a DIC PSF at the best focus plane: a) real and b) imaginary components generated using the model outlined in Sec 2.1, Eq. (1) for a 63x, 1.4 NA objective lens, 540nm illumination, shear 0.17 μm, bias π/4 radians, and a sampling distance between pixels of 0.1 μm.

The shear distance is set by the Nomarski prisms and objective lens used during imaging. Accurate determination of this distance is vital to proper modeling of the system and a method for determining that value is explored in Section 4.2. Introduction of a phase bias can be accomplished in one of three ways: laterally shifting the analyzer Nomarski prism, introducing a quarter wave plate to the system and rotating the analyzer (de Senarmont configuration), or more recently through the use of liquid crystal (LC) bias cells as explored as a portion of this thesis. The use of LC bias cells is preferred as it is the most accurate, flexible, and quantifiable of the methods. A technique for calibrating the LC bias cells for this purpose is covered in Sec 4.1. Lastly, the amplitude ratio *R* is determined by the relative alignment of the polarizer and analyzer. When imaging phase objects it is typically 0.5 which represents orthogonal polarization and is indicative of equal strength illumination for both polarized wave fronts.

It is helpful to view this model in the Fourier domain as well. This simplifies the implementation of the PSF model (discussed later in Section 3.1) as well as allowing some insight to the performance of the AM algorithm when analyzing its output in the Fourier domain. The PSF model outlined in Eq. (1) can be rewritten as its Fourier transform:

$$H(f,g) = -j\sin(2\pi f\Delta x + \Delta\theta)\,K(f,g), \tag{2}$$

where $K(f,g)$ is the coherent transfer function. This transfer function is the Fourier transform of a clear circular aperture which defines the frequency support of the system. The cutoff frequencies for $H(f, g)$ are $f_c = g_c = NA/\lambda$ where NA is the numerical aperture of the objective lens and λ is the wavelength of the illuminating light source.[3] The PSF shown in Figure 4 is recreated here showing its Fourier equivalent.

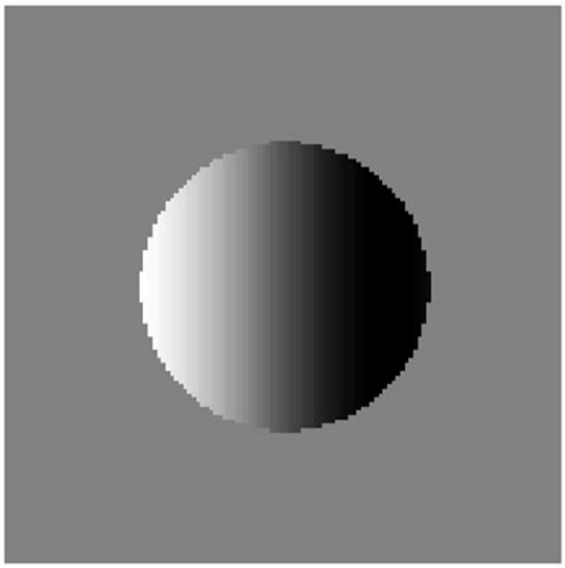

Figure 5. Imaginary component of Fourier domain representation of the DIC PSF shown in Figure 4. Model contains no real component.

2.3 Existing Algorithms for Object Reconstruction from DIC Images

There are numerous techniques for quantitative phase image with DIC microscopy[25] each with their own advantages and limitations. The selection is of course influenced heavily by which technique suits the application and end result desired for a given situation. As this thesis is focused on the Alternating Minimization Algorithm proposed by Preza and O'Sullivan, only two algorithms, SPI and RD-DIC, most relevant to that approach will be given any considerable attention. Preza's work on RD-DIC is of particular importance as it is the precursor to AMA and laid the groundwork for the system model being utilized. SPI is noteworthy as it also works based on a rotationally diverse data collection strategy and generates an isotropic linear phase estimation of the underlying specimen. This provides a good reference to assist in validating the results obtained with AMA when estimating phase objects.

2.4 Forward Imaging Model

The DIC PSF model given by Eq. (1) forms the basis for the forward imaging model used for the development of the AM algorithm. Defining a complex function $f(\boldsymbol{x})$ to represent the transmittance of the object being imaged allows a simplified imaging system to be modeled by the equations:[24]

$$f(\boldsymbol{x}) = |f(\boldsymbol{x})|e^{-j\pi\theta(x)} \tag{3}$$

$$i_k(\boldsymbol{x}) = a_k \left| \int_{-\infty}^{\infty} h_k(\boldsymbol{x} - \boldsymbol{x_o}) f(\boldsymbol{x_o}) d\boldsymbol{x_0} \right|^2 \tag{4}$$

where $\boldsymbol{x}$ is a collection of points representing a finite domain over which the image is defined, a_k gives the intensity of the illumination source, $h_k(\mathbf{x})$ is the DIC PSF for a given shear direction, $f(\boldsymbol{x})$ is the complex-valued object transmittance function, and $i_k(\boldsymbol{x})$ is the resulting intensity image, and *k* is an index indicating the shear direction. Additionally, we define $d_k(\boldsymbol{x})$ to represent the measured intensity images which can be either experimentally collected images or in the case of simulation a forward model intensity image based on the true numerical object.

The forward model is limited by the definition of the DIC PSF utilized. The Fourier transform of the PSF is limited entirely of lower frequency content defined by the circular support as can be seen in Figure 5. This gives rise to a null space in the forward imaging operator and prevents a direct inversion of the imaging process. Since high frequency components in the object transmittance function do not contribute to the final intensity image, it becomes necessary to account for this when computing an estimation of the object function. To achieve this, a roughness penalty, discussed in Section 2.5, is introduced to restrict differences between adjacent values within the object estimations to

acceptable ranges as defined by the strength of the penalty. This also has the added benefit of working to mitigate the influence that noise corruption of the measured data has on the final object estimations.

The imaging model, as described in Eq. (4), is defined over a finite support. It is important to also restrict the estimated object (i.e. a solution to the inverse imaging problem) to exist only within this support as well. This poses a challenge from a signal processing viewpoint when dealing with the boundary of the region over which the objects are defined. The boundary introduces a sharp edge where the object space transitions from an object surrounded by constant background intensity to an undefined space. This creates a sharp edge in the imaging space, which introduces undesirable artifacts when applying the forward model and trying to compute the solution to the inverse problem. To alleviate this issue two approaches are used:[8] 1) introducing a guard band around the image to mitigate edge artifacts that are unavoidable during the estimation process; and 2) subtracting the background intensity of the image that gets convolved with the PSF in order to reduce the discontinuity that it creates, and thus alleviating in this manner the majority of the artifact before it becomes a problem. The guard band implementation is simply a matter of operating on a smaller support when computing various steps of the algorithm. Shifting the intensity background is slightly more complicated and is accomplished by introducing new terms f_0, a known background constant in the object , and H_{k0}, the sum of intensities in the DIC PSF, in the forward model and expanding Eq. (4) to become

$$i_k(\boldsymbol{x}) = a_k \left| f_0 \int_{-\infty}^{\infty} h_k(\boldsymbol{x} - \boldsymbol{x_o}) d\boldsymbol{x_0} + \int_{-\infty}^{\infty} h_k(\boldsymbol{x} - \boldsymbol{x_o}) \left(f(\boldsymbol{x_o}) - f_0\right)] \, d\boldsymbol{x_0} \right|^2$$

$$= a_k \left| f_0 H_{k0} + \int_{-\infty}^{\infty} h_k(\boldsymbol{x} - \boldsymbol{x_o}) (f(\boldsymbol{x_o}) - f_0)] \, d\boldsymbol{x_0} \right|^2 \quad (5)$$

2.5 Solution to the Inverse Imaging Problem Using the AM Algorithm

The goal of the AM algorithm is to determine the complex valued object transmission function $f(x)$ that minimizes the objective function:[8]

$$\min_{f(\boldsymbol{x})} \sum_{k=1}^{2} \int_{\boldsymbol{x}} \left| \sqrt{d_k(\boldsymbol{x})} - \sqrt{i_k(\boldsymbol{x})} \right|^2 d\boldsymbol{x}. \quad (6)$$

As established before, $d_k(\boldsymbol{x})$ denotes the measured intensity of the experimentally collected data. Let $i_k(\boldsymbol{x})$ denote the result of applying the forward model from Eq. (5) to the current estimate of the complex valued object that we seek to determine given the measured data. In this representation $d_k(\boldsymbol{x})$ is a static real valued function that cannot be altered leaving only $i_k(\boldsymbol{x})$, a complex valued function, available to be altered so that the objective function is minimized. This results in an intractably large search space with a weak heuristic to inform the selection of reasonable object function estimations to satisfy the objective function in Eq. (6).

One common solution for difficult minimization problems is to derive a new representation of the objective function that is easier to minimize. This typically involves the introduction of a new variable or equation that allows the objective function to be rewritten. In this AM algorithm the use of the unmeasured phase of the data $d_k(\boldsymbol{x})$, defined as $\psi_k(\boldsymbol{x})$, is introduced to add an additional degree of flexibility. Since the values within $d_k(\boldsymbol{x})$ are strictly real-valued while the values in $i_k(\boldsymbol{x})$ are complex-valued,

it is impossible to make an informed choice on updates to the object. By adding this new unmeasured phase term it is possible to make informed decisions on object updates as both terms are now complex-valued. The objective function given in Eq. (6) is thus rewritten to become

$$\min_{f(\boldsymbol{x})} \min_{\psi_k(\boldsymbol{x})} \sum_{k=1}^{2} \int_{\boldsymbol{x}} \left| \sqrt{d_k(\boldsymbol{x})} e^{j\psi_k(\boldsymbol{x})} - \sqrt{a_k} \int h_k(\boldsymbol{x} - \boldsymbol{x_o}) f(\boldsymbol{x_o}) d\boldsymbol{x_0} \right|^2 d\boldsymbol{x}, \tag{7}$$

and includes an expansion of $i_k(\boldsymbol{x})$ to its form defined in Eq. (4). The derivation and validation of this altered representation can be found in previous publications[4] on the AM algorithm development.

The inclusion of a roughness penalty to Eq. (7) is an important aspect of this algorithm. Due to the ill posed nature of the inverse imaging problem, stemming from the limited frequency support of the PSF, it is possible for small changes in the imaged data to lead to large changes in the estimated complex object function. These large changes are contrary to the AM model because they represent high frequency information that is not transferred through the system in the forward model. This can lead to situations where the algorithm suggestions solutions of the objective function that are nonsensical. The penalty function, along with a constraining of estimation magnitudes, serves to regularize estimations explored by the algorithm. Placing a limit on the absolute value of the complex object data at each point along with limiting the maximum difference between neighboring pixels, reduces the search space and ensures the solutions tested are admissible.

There are many penalties suitable for this task. The main characteristic desired is a quadratic response for small changes and a linear response to larger changes. Penalties

that take this form approximate the Huber, or robust least squares, penalty.[26] For this algorithm a penalty based on a log cosh function was chosen, which roughly approximates the behavior of the Huber penalty, defined by

$$\rho(x) = \delta \ln \cosh\left(\frac{x}{\delta}\right). \tag{8}$$

This penalty is applied to neighboring pixels resulting in the extended definition

$$P\big(f(x)\big) = \sum_{k,l} \rho(|f(k,l) - f(k+1,l)|) + \rho(|f(k,l) - f(k,l+1)|)\,, \tag{9}$$

which has the undesired consequence of introducing a dependency between neighboring pixel values. A workaround to decouple neighboring pixel values, thus allowing the algorithm to update individual sample points, is outlined in literature[7, 8] and results in a new representation of the penalty function in terms of its derivative:

$$\begin{aligned}\frac{\partial}{\partial f} P\big(f^{(m+1)}\big) = \sum_{S} \delta \tanh\left(\frac{\left|2f^{(m+1,i)}(k,l) - f^{(m)}(k,l) - f^{(m)}\big(S(k,l)\big)\right|}{\delta}\right) \\ \times\ exp\left(-j * arg\left(\left|2f^{(m+1,i)}(k,l) - f^{(m)}(k,l) - f^{(m)}\big(S(k,l)\big)\right|\right)\right)\end{aligned} \tag{10}$$

where *m* is the current algorithm iteration, *i* is a sub iteration allowing multiple applications of the penalty, and *S* is the set of adjacent pixels (above, below, left, and right) to the pixel being processed for the penalty. A guard band around the outside edge of the imaging space is utilized in the implementation of this equation to ensure the sampling of neighboring pixels is always done within a region that contains information relevant to the current estimation.

Explanation of the algorithm requires first defining a few variables and sets to simplify expressions. As the algorithm works on a discretized representation of the image and object spaces, let **n** be the data points in the imaging space and **i** be the data

points in the object space. Additionally, domains Γ and Ω are utilized and represent the complete object space and the sub region after removal of a guard band respectively. Algorithm convergence parameters $\alpha(\mathbf{n})$ and $\gamma(\mathbf{i})$ are precomputed per techniques outlined and compared in Section 3.4. All subscripts *k* denote the rotationally diverse datasets and take values 1 or 2, while superscripts *m* denote iteration number. Finally an initial guess for the unobserved phase data ${\psi_k}^{(0)}(\mathbf{n})$ and the complex object function $f^{(0)}(\mathbf{i})$ are made. With these values defined, the AMA operates by solving the following iterative algorithm:

$$
\begin{aligned}
s_k^{(m)}(\mathbf{n}) &= \sqrt{d_k(\mathbf{n})}e^{j\psi_k^{(m)}(\mathbf{n})},\ k=1,2,\ \mathbf{n}\in\Omega \\
g_k(\mathbf{n}) &= s_k^{(m)}(\mathbf{n}) - f_0 H_{k0},\ k=1,2,\ \mathbf{n}\in\Omega \\
e_1(\mathbf{i}) &= \gamma(\mathbf{i})\sum_{k=1}^{2}\sum_{\mathbf{n}\in\Omega} h_k^*(\mathbf{n}-\mathbf{i})\left[g_k(\mathbf{n}) - \sum_{\mathbf{i}'\in\Gamma} h_k(\mathbf{n}-\mathbf{i}')\left(f^{(m)}(\mathbf{i}') - f_0\right)\right] \\
f_u(\mathbf{i}) &= f^{(m)}(\mathbf{i}) \\
e_2(\mathbf{i}) &= \kappa\frac{\partial}{\partial f}P^{(m)}(f_u)(\mathbf{i}) \\
f_u(\mathbf{i}) &= f^{(m)}(\mathbf{i}) + e_1(\mathbf{i}) + e_2(\mathbf{i}) \\
f_u(\mathbf{i}) &= \frac{f_u(\mathbf{i})}{\max(1, |f_u(\mathbf{i})|)} \\
f^{(m+1)}(\mathbf{i}) &= f_u(\mathbf{i}) \\
\psi_k^{(m+1)}(\mathbf{n}) &= \arg\left((1-\alpha_k(\mathbf{n}))\left(f_0 H_{k0} + \sum_{\mathbf{i}\in\Gamma} h_k(\mathbf{n}-\mathbf{i})\left(f^{(m+1)}(\mathbf{i}) - f_0\right)\right) + \alpha_k(\mathbf{n}) s_k^{(m)}(\mathbf{n})\right)
\end{aligned}
$$

which serves to minimize the objective function in Eq. (7). It begins with defining ${s_k}^{(m)}(\boldsymbol{n})$, the complex valued data based on the measured DIC image using an estimation of the unobserved phase component of that data. This is shifted to remove the background component in the same manner as outlined in Eq. (5). The forward model is then applied to the current object estimate and the result is removed from $g_k(\boldsymbol{n})$. This difference is again put through the forward model, using the conjugate of the PSF (the computation of the adjoint operator), resulting in $e_1(\mathbf{i})$ a guess of the update required for

the estimate solution of the object. Next the penalty is applied to the current object function and yields $e_2(\mathbf{i})$. These are added to the current object function estimate to produce an updated object function. The magnitude constraint is enforced on the new estimation of the complex valued object function.

Up to this point in the process the estimate of the unobserved phase data has been held constant and an attempt to minimize the object function has been computed. To compute the other side of the alternating minimization, the object function is now held constant and an attempt to estimate the unobserved phase data is now computed. By applying the forward model to the new estimated object function and adding ${s_k}^{(m)}(\boldsymbol{n})$, the previous combination of true observed data and estimated phase, we obtain a new estimation of the unobserved phase mask based on the new object estimation. Repeating these steps yields a converging estimation of the true object function by continually finding the error in a previous estimation, either of the complex valued object function or of the unobserved phase, and adjusting for it then iterating again until convergence.

CHAPTER 3

APPLICATION OF AMA TO SIMULATED DIC DATA

Applying the algorithm to simulated data is an important step in the development of the computational model. It allows the removal of many of the difficulties faced when working with experimental data such as noise, data registration, determining physical system properties from the process. Instead focus can be placed on validating the system model, numerical object specification, and in ensuring the algorithm behaves as intended and can reproduce simulated inputs accurately. This Section focuses on using these advantages to improve the implementation of the algorithm. First an improvement to the DIC PSF model is demonstrated in Section 3.1 followed by the use of this improvement to generate simulated bead objects that accurately reflect experimental data. Next, a new set of algorithm parameters is discussed in Section 3.3. The Section concludes with the use of the new parameters and the roughness penalty to determine appropriate penalty weights to use under varying levels of noise.

3.1 Creation of Rotationally-Diverse DIC Point Spread Functions

The derivation of the PSF model utilized for this study is detailed in Sec 2.2 and results in Eqs. (1) and (2). For purposes of generating a PSF it is easier to work with the Fourier domain equivalent given by Eq. (2) in addition to improving the quality of the end result in cases involving shear directions not along a primary axis. The setup of each PSF is dependent upon the physical characteristics of the objective lens, camera sensor, and Nomarski prisms. These are used to determine the frequency cutoff of the system which determines the size of the aperture on which the PSF is defined. The size of

individual pixels on the camera sensor is also vital as it determines the final sampling interval at which the PSF should be represented.

Proper sampling is one of the main challenges faced in the creation of a DIC PSF using this model. Representing a continuous function in a discrete manner introduces a chance for error due to changes in the distribution of intensity values. This factor is mitigated to some degree by first computing a highly sampled version of the PSF on a larger grid than desired and then down sampling it to the size required for data processing. This process results in a smoother approximation of the true PSF.

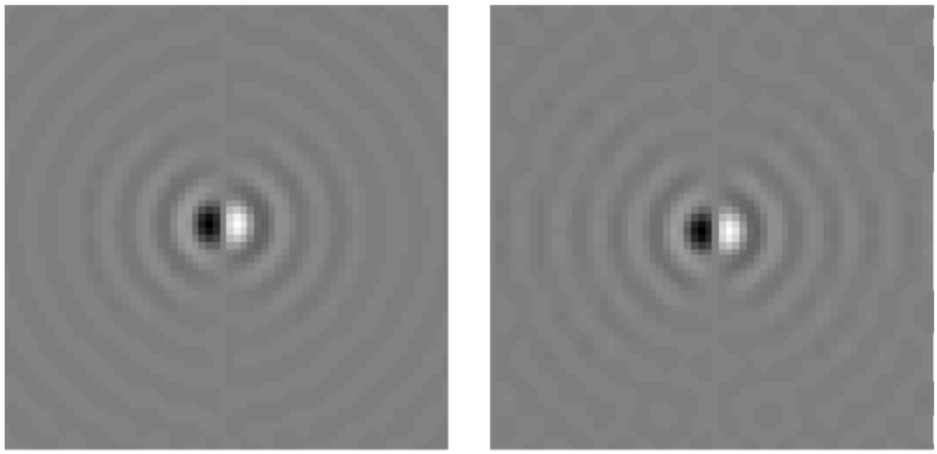

Figure 6. Demonstration of the effects of sampling approaches on final result of PSF formation showing a) real portion of a PSF created at 0.17μm sampling on a 128x128 grid then interpolated to effectively be sampled 0.34 μm on a 64x64 grid and b) the same PSF created at 0.34 μm sampling on a 64x64 grid. Both PSFs are based on a 10x/0.3 NA lens, 540-nm illumination, shear 0.34 μm, and bias of $\pi/2$.

Another important step in the PSF creation process is the rotation of each PSF to match the desired direction of shear. Generally data will be collected so the shear aligns with the major axes, one collection with shear oriented horizontally and a second with

shear oriented vertically. If, however, the data is collected and exhibits a shear along some other direction, it is necessary to create PSFs that reflect this. Originally this was performed as a final step in the creation process where the PSF is simply rotated spatially. This approach works fine for the assumed cases above with shear along a major axis. When shear along an arbitrary direction is desired spatial orientation was found to provide a poor approximation of the desired PSF (see Figure 7).

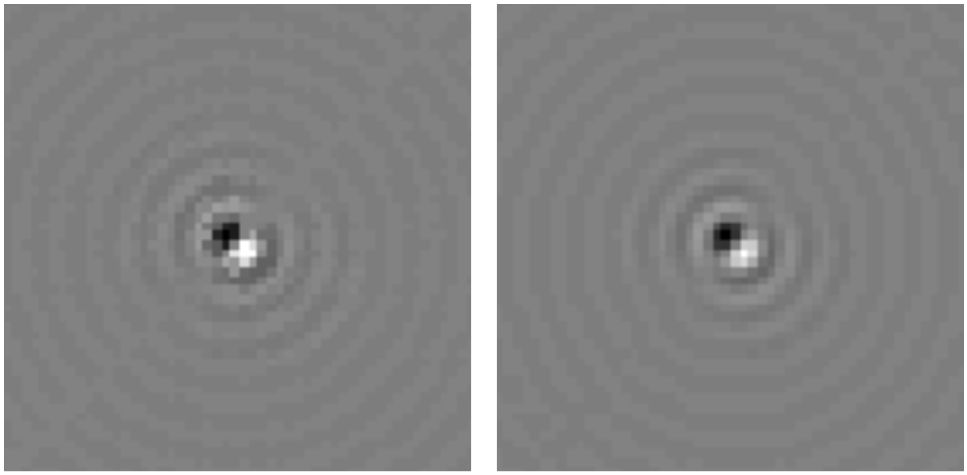

Figure 7. Demonstration of a) artifacts and poor resampling of DIC PSF when rotated spatially and b) improved qualitative appearance and symmetry in DIC PSF rotated in Fourier domain. Both PSFs are indicative of a 63x/1.4 NA objective lens with bias $\pi/4$, shear 0.17 μm, sampling 0.1 μm, and illumination of 540 nm.

Even distribution of energy in the two sheared wave fronts is important to the proper functioning of DIC microscopy (Eq. (1)). This ensures the returned phase encoding is a proper derivative along the shear direction and does not give undue weighting to the object position sampled by one wave over its coherent pair. As can be seen in Figure 7a the spatial rotation approach utilized does not result in an image with an

even distribution of energy between the two points nor does each point have the same uniform and quasi-symmetric shape as seen in Figure 6. To alleviate this anomalous appearance, the implementation of the rotation step was moved to occur in the Fourier domain. This is possible because the Fourier transform is rotationally invariant.

As shown earlier (Eq. (2) and Figure 5), the representation of the PSF in the Fourier domain is entirely on a circular support and it is a sinusoidal modulation along the direction of shear. These two features make it possible to perform a rotation of this representation of the PSF without destroying any of the underlying features or relations in neighboring values. The end result is a spatial PSF rotated to the desired shear direction, shown in Figure 7b, and without the undesirable artifacts and asymmetry seen in Figure 7a.

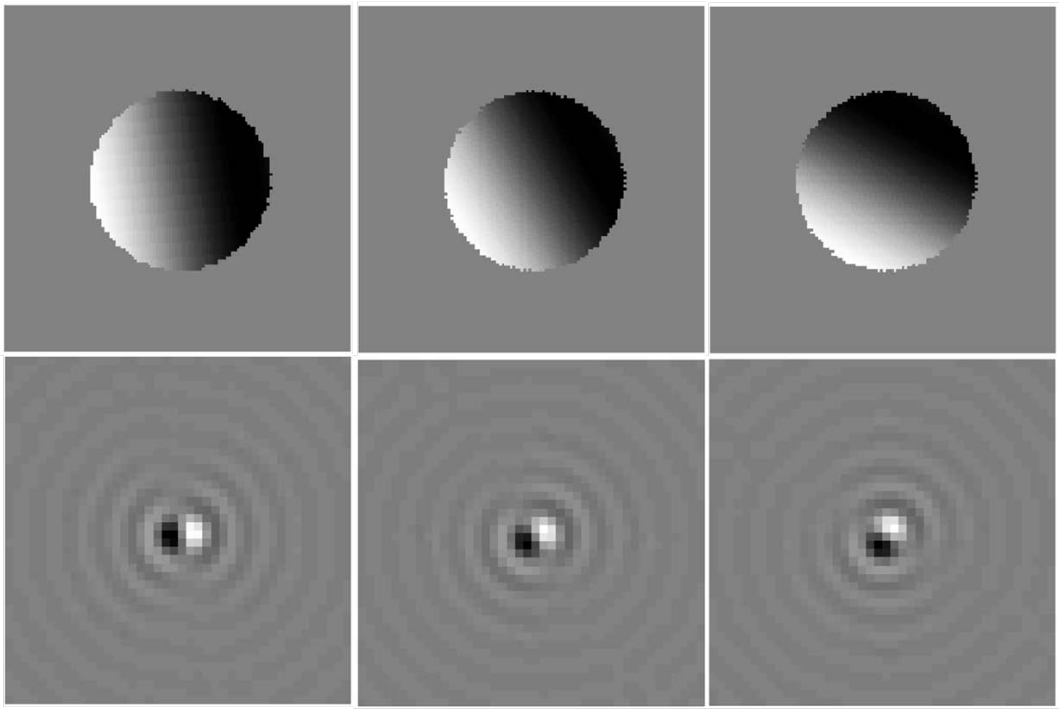

Figure 8. Three DIC PSFs with an off axis shear direction: a) 10 degrees, b) 30 degrees, and c) 60 degrees, respectively, with respect to the horizontal axis. Top row: imaginary component of Fourier domain representation of the PSF. Bottom row: real component of DIC PSF in spatial domain. All PSFs are indicative of a 63x/1.4 NA objective lens with bias $\pi/4$ radians, shear distance 0.17 μm, and sampling distance between pixels 0.1 μm.

3.2 Selection of Simulated Objects and DIC Data Generation

Testing the algorithm in simulation requires the creation of simulated DIC images utilizing the forward model outlined in Section 2.4. Doing this requires the creation of a simulated object. A numerical "blob" object was created to serve this role. It has a non-uniform magnitude and phase and an irregular shape and can be seen in Figure 9. The values for the phase were chosen to be representative of what could be expected from a real sample that would be experimentally imaged. They are based upon the formula defining the optical path length experience by light propagating through the object

$$OPL = \phi(x) = \frac{2\pi(n_2 - n_1)t}{\lambda}, \tag{11}$$

with n_2 being the refractive index of the object's structure, n_1 the refractive index of the mounting medium, t is the thickness of the sample, and λ the wavelength of the illuminating light. Assuming a sample thickness of 1μm, λ=550nm, and refractive index mismatch of roughly 0.035 yields maximum phase values of 0.4 radians and background values of 0 radians. The magnitude of the blob is defined, for simplicity, to be directly related to the phase by

$$|f(x)| = 1 - c\phi(x), \tag{12}$$

where c is a constant controlling absorption strength, yielding background values of 1 representing no absorption of light and increasing absorption with increasing phase content.

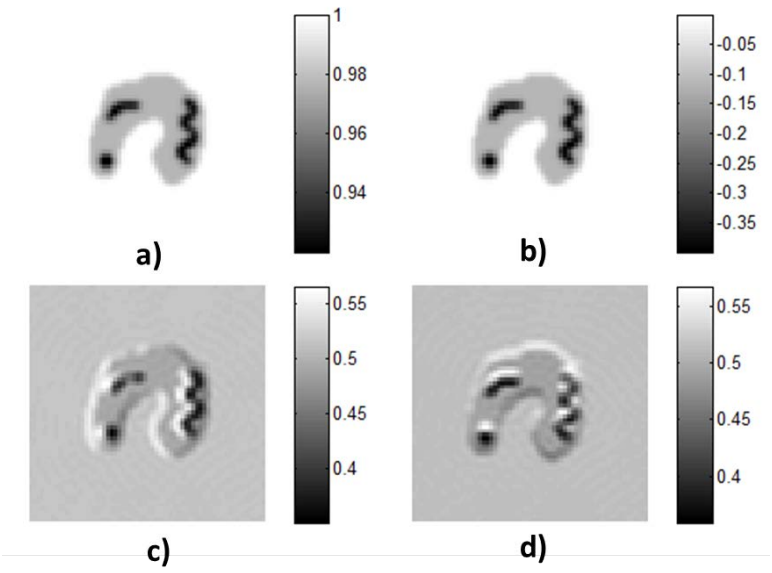

Figure 9. Example of the simulated blob object a) magnitude, b) phase, c) forward model DIC image with shear direction at 0 degrees, and d) forward model DIC image with shear direction at 270 degrees with respect to horizontal axis. Generated using 10x/0.3 NA lens, 0.34 µm shear distance, 0.34 µm sampling, and $\pi/2$ bias at 540 nm illumination.

A second simulated object was created to assist in validating the algorithm for use with experimental data. This object is an approximation of a 6µm in diameter fluorescent polystyrene ring bead typically utilized for fluorescence microscopy research. These beads are solid with a spherical shell of dye embedded along the surface. This dye shell extends roughly 0.5 µm to 0.6 µm down from the surface. This causes the bead to exhibit an absorption profile mimicking the dyed portion while maintaining a constant, uniform phase component as shown in Figure 10. The refractive index of the bead is 1.53 and the medium in which the bead was mounted has a refractive index of 1.56.

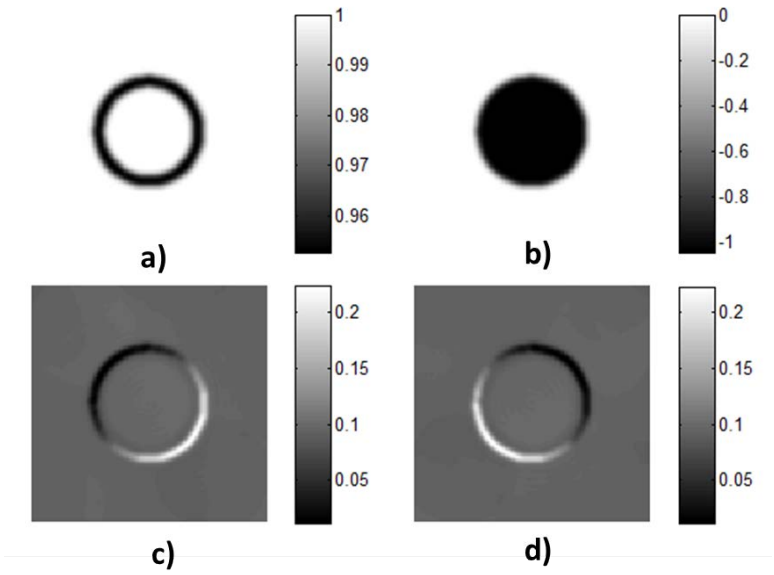

Figure 10. Example of the simulated 6μm in diameter polystyrene fluorescent bead a) magnitude, b) phase, c) forward model DIC image with shear direction at 135 degrees, and d) forward model DIC image with shear direction at 45 degrees with respect to horizontal axis. Generated using a 63x/1.4 NA lens, 0.17 μm shear distance, 0.1 μm sampling distance, and π/4 bias at 540-nm illumination.

3.3 Investigation of AMA Parameters with Simulations

The discussion in Section 2.5 detailing the theory of the AM algorithm includes an approach for applying a magnitude constraint on the estimated data. This involves the expansion of the algorithm to include additional terms to simplify the decoupling of the estimated parameters allowing a simplified imposition of this and other constraints. This process introduced additional parameters defined as α, β, and γ (which are not single constants and thus are represented as vectors)[8]. It should be noted that all three parameters are present only in previous versions of this algorithm. Recent investigation utilizes an approach relying only upon α and γ, with β =1. Selection of these values

directly influences the convergence rate of the algorithm and must be given careful consideration. An iterative approach for optimizing these choices based on solving the system of equations

$$Diag(\mathbf{H^T BHGH^T BH}) = Diag(\mathbf{H^T BH}) \tag{13}$$

$$Diag(\mathbf{HGH^T BHGH^T}) = Diag(\mathbf{HGH^T}) \tag{14}$$

was proposed and investigated.[7] In these equations **H** is the convolution kernel utilized in the forward model computation and **B** and **G** are diagonal matrices representing the β and γ parameters respectively. Early results applied to noiseless simulation were promising as shown in Figures 11 through 14; however there are some limitations to this approach.

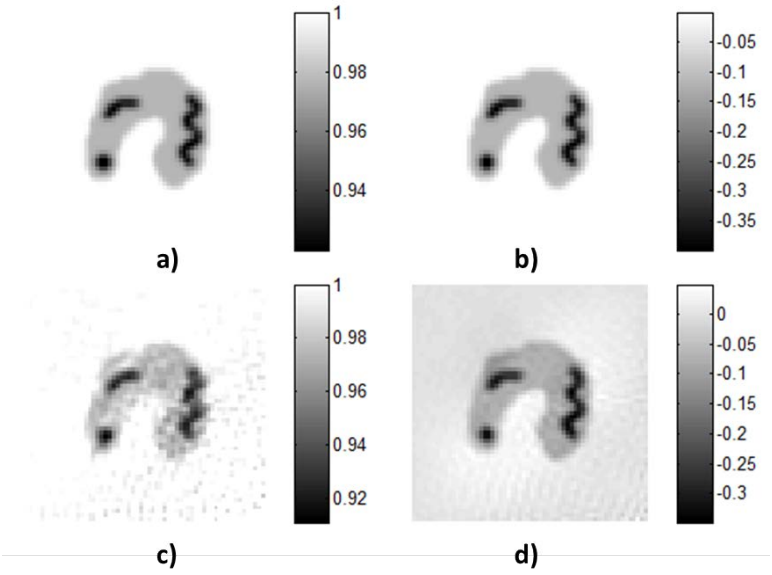

Figure 11. Results of running AMA on simulated blob object data using α, β, and γ parameters computed using Eqs. (13) and (14) showing: a) true magnitude, b) true phase, c) estimated magnitude, and d) estimated phase after 3,000 iterations.

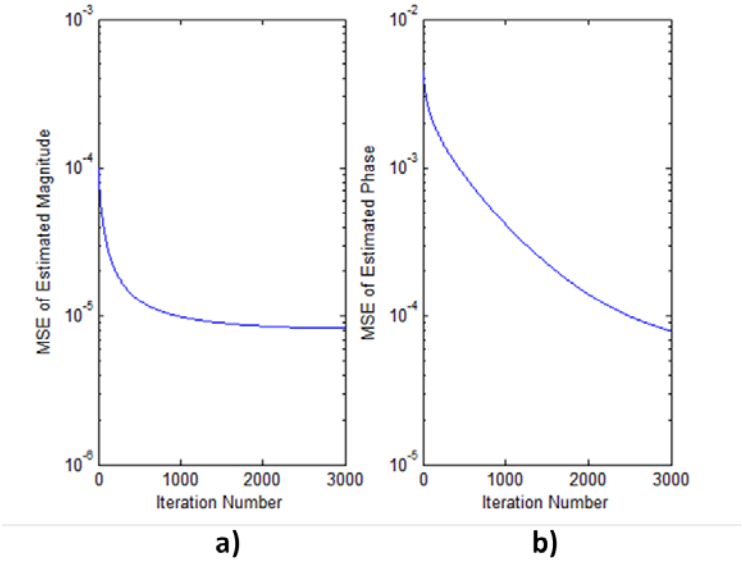

Figure 12. Error curve for object estimations in Figure 11 showing Mean Square Error (MSE) between true numerical object and AMA estimation for a) object magnitude and b) object phase.

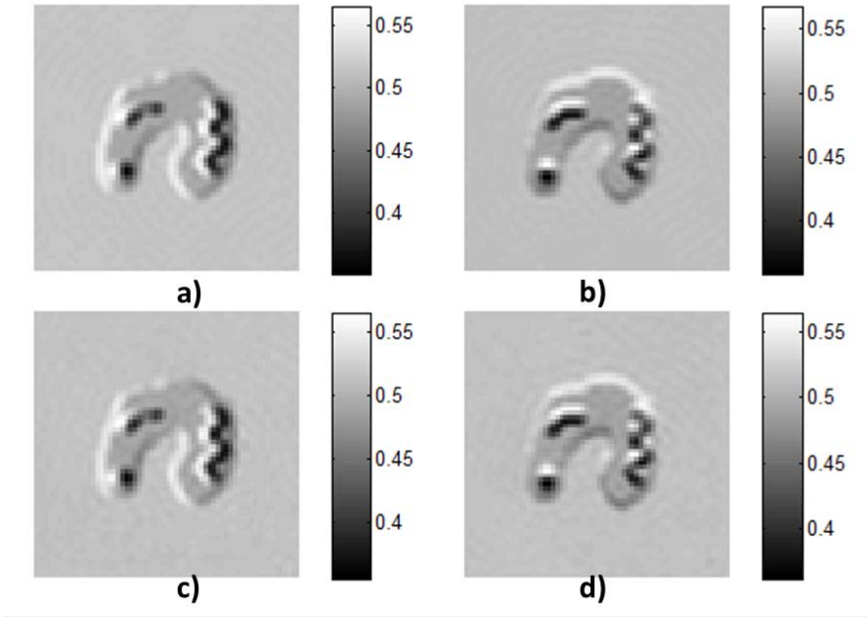

Figure 13. Forward model results for simulated blob object in Figure 11: (a & b) forward model images for true object at orthogonal directions of shear and (c & d) forward model images for estimated object. Left column shows shear direction 0 degrees and right column shows shear direction 270 degrees. Forward model computed using 10x/0.3 NA lens, 0.34-μm shear distance, sampling distance of 0.34 μm, and bias $\pi/2$ radians at 540 nm illumination.

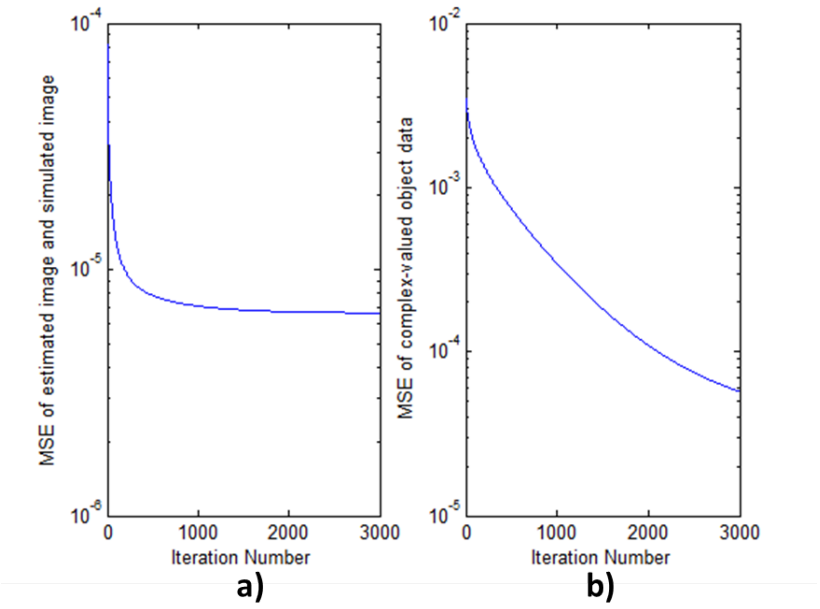

Figure 14. Error curves for forward model images in Figure 13 showing the MSE between a) the difference in forward model of the true numerical object and forward model of the final estimated object and b) the absolute value of the difference between the complex valued true numerical object and final estimation. These curves show how the object continues to change despite the forward model having converged showing the ill-posed nature of the system.

The solution of Eqs. (13) and (14) involves solving an iterative minimization problem. This search is computationally costly when working on datasets of any significant size and is not guaranteed to converge for any given convolution kernel. A more stable and quickly computable approximation is desired. Through collaboration with Dr. O'Sullivan (Professor of Electrical and Systems Engineering at Washington University in St. Louis), the following derivation was made:

$$(f^* - f^{n+1}) = GH^T H(f^* - f^n)$$

$$G = \frac{(H^T H)^{-1}(f^* - f^{n+1})}{(f^* - f^n)}$$

$$G = \frac{(H^T H)^{-1}}{w} \tag{15}$$

where f^* is the preliminary estimation of the object function, f^n and f^{n+1} are the constrained estimates of the object at iterations *n* and *n*+1, **H** is the convolution kernel, and **G** is a matrix whose elements are the values of parameter γ. Values for parameter α are set to a constant chosen through an empirical study, which showed its value did not have a significant effect on the outcome. Parameter β is set to 1 to remove its influence in the computations. This allows easily switching between new and old equation sets without requiring a reimplementation of the model. This also simplifies algorithm analysis as the only parameter changing is γ. Figures 15 through 18 show results of running the algorithm with the parameter set in Eq. (15) under the same simulation conditions as in Figures 11 through 14 which utilize Eqs. (13) and (14).

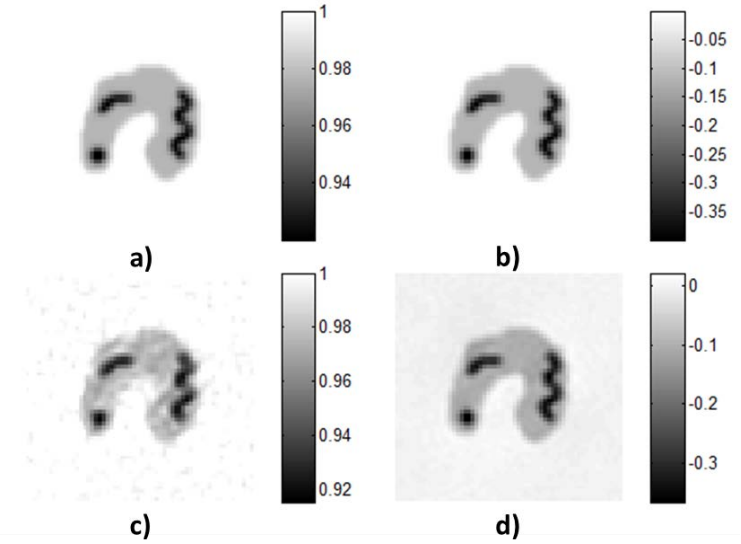

Figure 15. Results of running AMA on simulated blob object using $\alpha = 0.45$, $\beta = 1$, and γ was computed using Eq. (15) showing a) true magnitude, b) true phase, c) estimated magnitude, and d) estimated phase after 3,000 iterations of the AM algorithm.

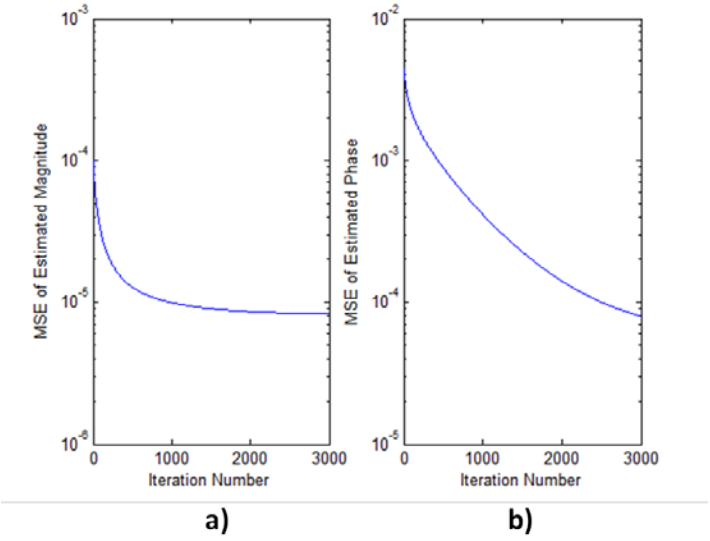

Figure 16. Error curve for object estimations in Figure 15 showing Mean Square Error between true numerical object and AMA estimation for a) object magnitude and b) object phase.

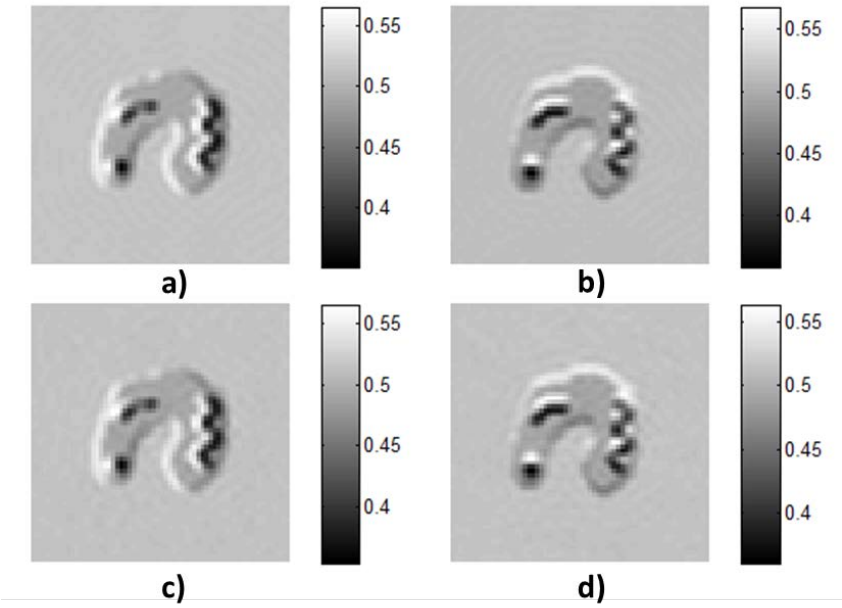

Figure 17. Forward model results for simulated blob object in Figure 15 showing a-b) forward model images for true object and c-d) forward model images for estimated object. Left column shows shear direction 0 degrees and right column shows shear direction 270 degrees with respect to horizontal axis. Forward model computed using 10x/0.3 NA lens, shear distance 0.34 µm, sampling distance of 0.34 µm, and bias of $\pi/2$ radians at 540 nm illumination.

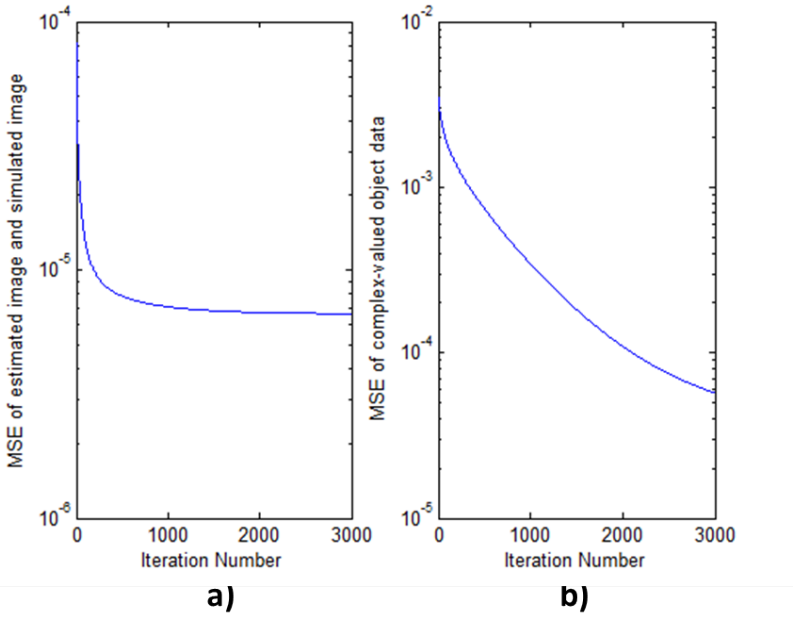

Figure 18. Error curves for forward model images in Figure 17 showing the MSE between a) the difference in forward model of the true numerical object and forward model of the final estimated object and b) the absolute value of the difference between the complex valued true numerical object and final estimation. These curves show how the object continues to change despite the forward model having converged showing the ill-posed nature of the system.

3.4 AMA Performance with Noisy Simulation

Proper simulation of microscope imaging requires accounting for noise sources present within the system. In order to ensure the synthetic DIC images used when working with simulated data properly reflect true experimental data they are corrupted with additive White Gaussian noise. The standard deviation of the noise was set to be between 0.5% and 2% of the maximum intensity present in the original uncorrupted simulated image. A Gaussian distribution was utilized due to the strong illumination possible with DIC imaging causing the modality to not be a photon limited system. The low standard deviation is chosen to properly reflect the characteristic low noise

corruption present when using a high grade scientific CCD camera.[7] Images of noiseless and noisy synthetic images are shown in Figure 19. The level of noise is described by the ratio of the total intensity present in the image to the variance of the noise mask applied (aka as SNR) and it is expressed in decibels.

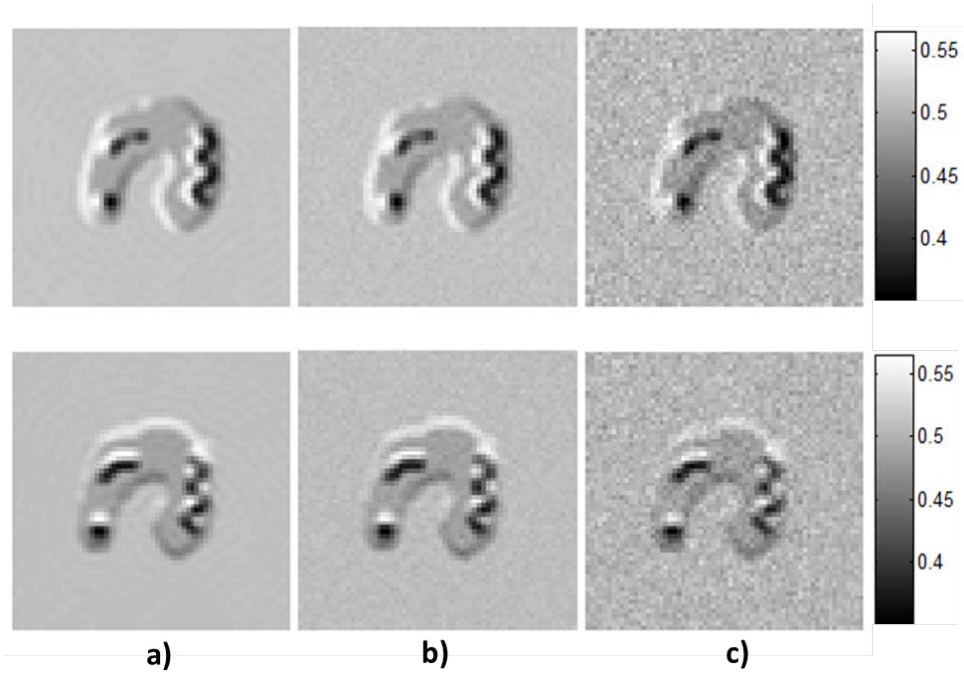

Figure 19. Images of simulated blob object demonstrating noise corruption with different amounts of noise and SNR: a) no noise, b) SNR of 45 dB (very low noise), and c) SNR of 35 dB (moderate noise). Top row contains images with shear direction of 0 degrees; bottom row contains images with shear direction of 270 degrees. Generated using 10x/0.3 NA lens, shear 0.34 μm, sampling distance 0.34 μm, bias $\pi/2$ radians, and 540-nm illumination.

The existence of noise introduces features to the imaging space that are not characteristic of the underlying object being sampled. This introduces potential errors in the object estimations being computed that lead to erroneous final results. To mitigate the influence of noise on the algorithm's estimations, a roughness penalty has been

proposed as detailed in Sec 2.5 and Eq. (10). A key term in the penalty is the penalty weight κ which governs the strength of the applied penalty. This adjustment parameter serves to allow a weaker penalty to be utilized in the presence of low noise levels and a stronger penalty to be utilized when strong noise is present. The penalty encourages results with smoother appearances which is a good trait when working on highly noisy data. This can lead to washed out and over smoothed final estimations. A tradeoff must be made between loss in fidelity of the object estimation and noise mitigation gained by the penalty's application.

Previous work by Preza and O'Sullivan[6-8] explored appropriate penalty values to use in simulation when introducing varying levels of noise. These prior works focused on the application of the penalty when utilizing AM algorithm convergence parameters as computed by the algorithm given by Eqs (13) and (14) in Section 3.3. The transition to a convergence model governed by Eq. (15) necessitated reinvestigation of these parameter choices. This is achieved by creating a dataset corrupted with a specified level of noise and running the algorithm with a broad range of κ values to determine a general range in which acceptable results can be achieved as measured by the MSE between the true object and the estimation produced by the algorithm. A more focused search can then be performed to determine the specific value that provides the best noise mitigation without over smoothing the estimated results. Figures 20 and 21 show the resulting object estimations and simulated DIC images for this investigation.

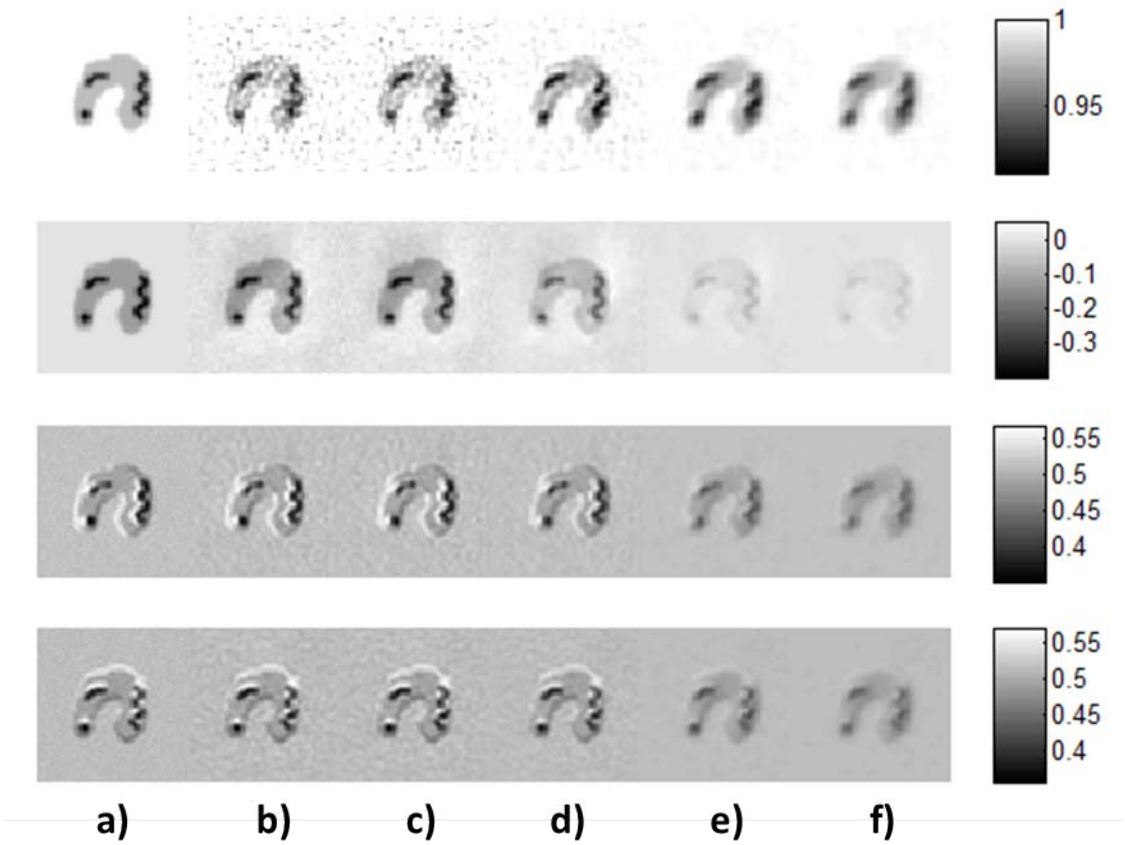

Figure 20. Analysis of the effects of increased penalty weighting on AMA estimations at 45 dB SNR. Top row shows object magnitude, second row shows object phase, and the bottom two rows show the forward model DIC images resulting from the object estimations. The first column (a) shows the true object and noisy forward model DIC images, the remaining columns show the results for varied κ values b) $\kappa = 0.004$, c) $\kappa = 0.005$, d) $\kappa = 0.05$, e) $\kappa = 0.5$, and f) $\kappa = 1$. Lens 10x/0.3 NA, sampling 0.34 μm, shear 0.34 μm, bias $\pi/2$, illumination 540 nm. $\alpha = 0.45$, $\beta = 1$, and γ was computed using Eq. (15).

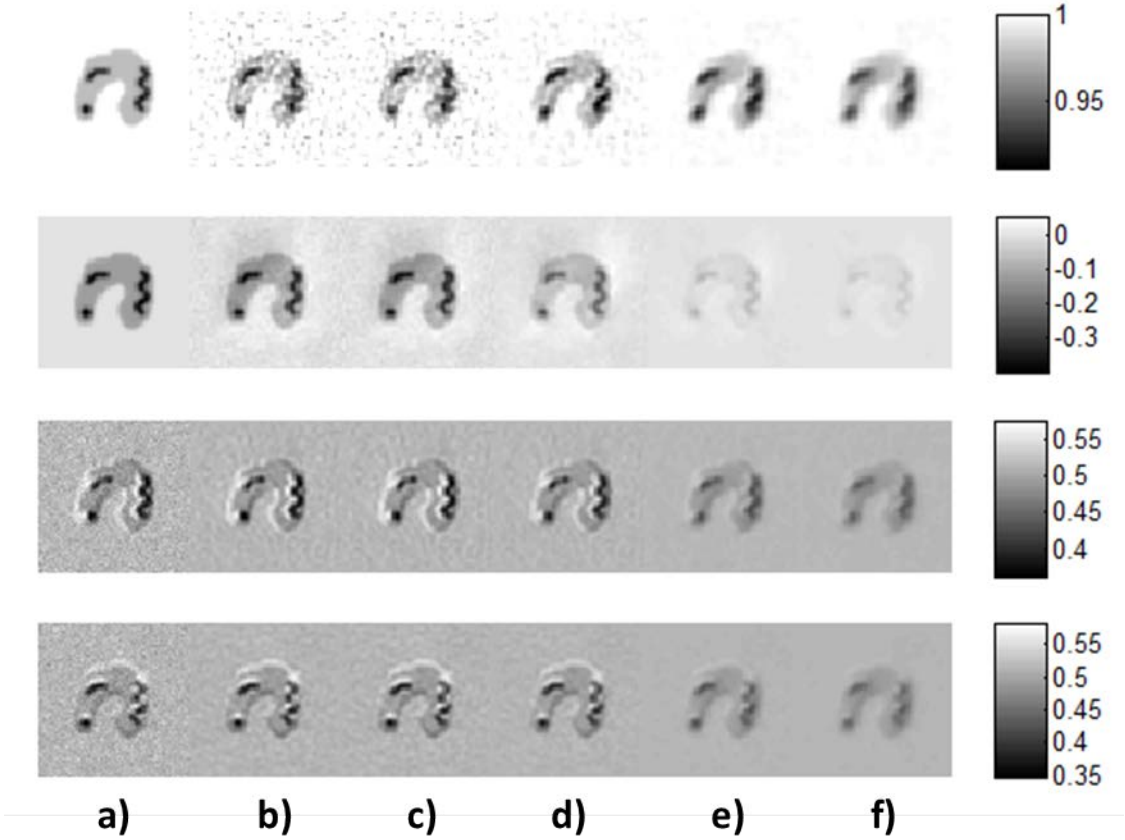

Figure 21. Analysis of the effects of increased penalty weighting on AMA estimations at 35 dB SNR. Top row shows object magnitude, second row shows object phase, and the bottom two rows show the forward model DIC images resulting from the object estimations. The first column (a) shows the true object and noisy forward model DIC images, the remaining columns show the results for varied κ values b) $\kappa = 0.004$, c) $\kappa = 0.005$, d) $\kappa = 0.05$, e) $\kappa = 0.5$, and f) $\kappa = 1$. Lens 10x/0.3 NA, sampling 0.34 μm, shear 0.34 μm, bias $\pi/2$ radians, illumination 540 nm. $\alpha = 0.45$, $\beta = 1$, and γ was computed using Eq. (15).

As can be seen, the penalty weighting has a large influence on the final estimated data and images. Higher values result in over smoothed and attenuated results as evident in the phase estimates in Figure 20 e) & f). Low values of the penalty do not properly mitigate the noise deterioration as can be seen in Figure 21 b) & c). Selection of a proper weighting for a given level of noise will ensure the best results possible are achieved. In order to quantify what constitutes a 'proper weighting' a study involving combinations of many weightings with simulated images corrupted by increasing noise levels was performed. This involved the creation of simulated images at 30, 35, 40, 45, 50 dB of noise, some of which are shown in Figure 19. These were run through the AM algorithm using κ values at each order of magnitude from 1e-5 to 10. Working with simulated objects allows for a direct comparison of the current estimate to the true object function. To evaluate performance of each penalty weighting at a given noise level, the MSE between the true and estimated object phase was computed along with the MSE between the true and estimated object magnitude. The best results from that set, judged using the computed MSE, were obtained for $\kappa = 0.01$. At $\kappa = 0.001$ the algorithm failed to converge and at $\kappa = 0.1$ the estimated images and object function were noticeably over smoothed. This trial study provided lower and upper bounds for values to be investigated further. A second trial was executed for κ values equal to 0.003, 0.007, 0.01, and 0.03, respectively, which further narrowed the search space to fall within the range of values 0.003 and 0.007. A final trial was computed sweeping κ from 0.001 to 0.01 in increments of 0.001 to ensure no possibilities were missed.

Shown below in Figure 22 are the results of this analysis using the MSE of the final iteration as a metric for determining the best weighting for a given noise level.

Results for 35 dB and 45 dB are shown. The final κ selections for each noise level are given in Figure 23. It is apparent from these results that the penalty weight is fairly constant for low levels of noise, roughly $\kappa = 0.005$, and only needs to be increased when the noise reaches moderately high levels.

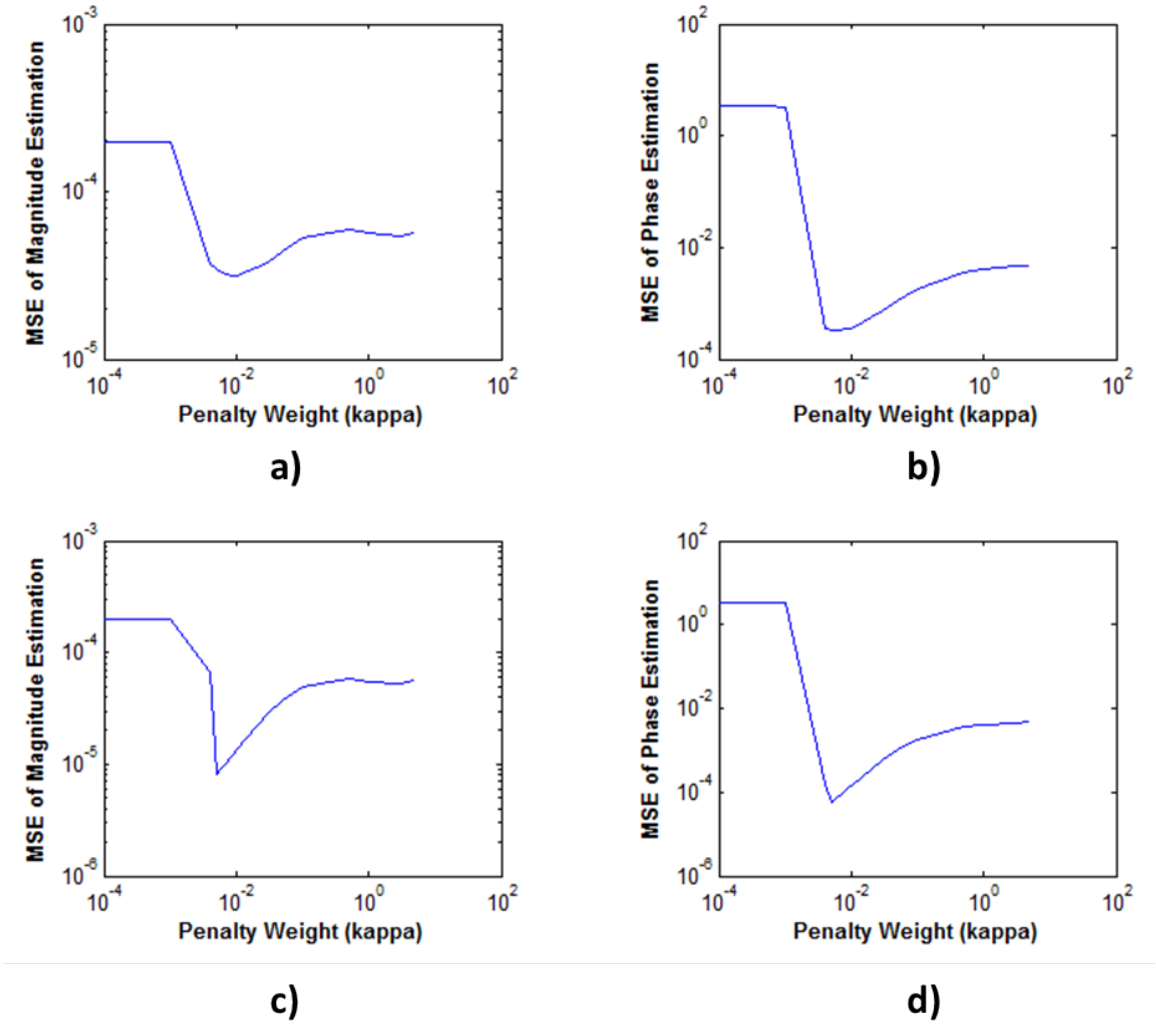

Figure 22. Results of penalty weight analysis under varying levels of noise for 35 dB and 45 dB SNR simulated datasets. Graphs show the final MSE for a given κ value for a) magnitude of object function at 35 dB SNR, b) phase of object function at 35 dB SNR, c) magnitude of object function at 45 dB SNR, and d) phase of object function at 45 dB SNR.

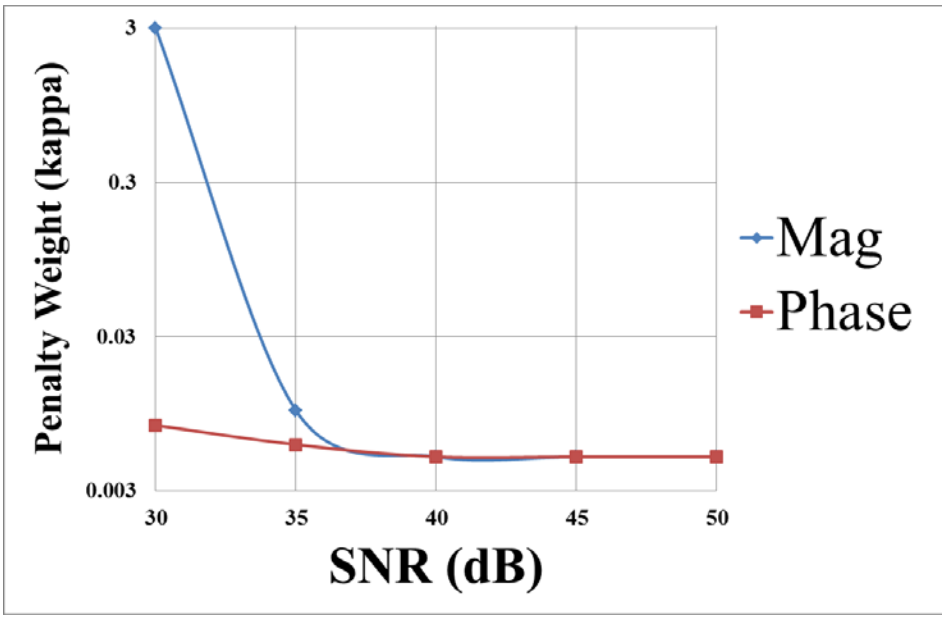

Figure 23. Final selection curve for the penalty weight κ at various SNR levels.

CHAPTER 4

APPLICATION OF AMA TO EXPERIMENTAL DATA

Transitioning from simulated data to experimentally gathered data poses many challenges. The forward model computations in the algorithm are simplified approximations of data acquired with the real system. This immediately introduces a source of error that cannot be circumvented. Effort must be taken to mitigate these discrepancies between the model being used and the actual system used to collect the data. The use of a calibrated liquid crystal bias cell is one step introduced to help increase the accuracy of the model used in the algorithm and is discussed in Sections 4.1 to 4.3. Using traditional DIC imaging setups, bias retardation is adjusted by sliding the objective Nomarski prism laterally within the light path. This is done manually and causes the exact bias retardation to be unknown. The devices are not calibrated and the exact slider position is difficult to reproduce. Knowing the exact amount of bias introduced by the system, made possible through the use of liquid crystal devices, along with the shear distance (determined experimentally as described in Section 4.3) created by the Nomarski prisms is vital to achieving the best results possible. These system additions are utilized to gather new experimental bead data as covered in Section 4.4. New preprocessing techniques are applied to this data (Section 4.5) and then the data is processed using both the AM algorithm and Spiral Phase Integration.

4.1 Description of Liquid Crystal Bias Cell Operation

The bias cell itself is composed to two sheets of optical grade glass with a thin layer of liquid crystal material between them and electrodes attached to the sides as shown in Figure 24. The crystals do not form one solid structure; instead they are a

collection of smaller crystalline lattices. These individual lattices arrange themselves into their lowest energy state. When a voltage is applied across the electrodes, the low energy state changes and the crystalline structures reorient in response. This response is non-linear and necessitates calibration of the device which is covered in Section 4.2. The refractive index experienced by a light wave is dependent upon both the polarity of the light and the current alignment of the crystalline lattices. Changes in alignment alter the effective refractive index experienced by the light waves.[21] This effect, shown in Figure 25, is the phenomenon that creates bias retardation within the system.

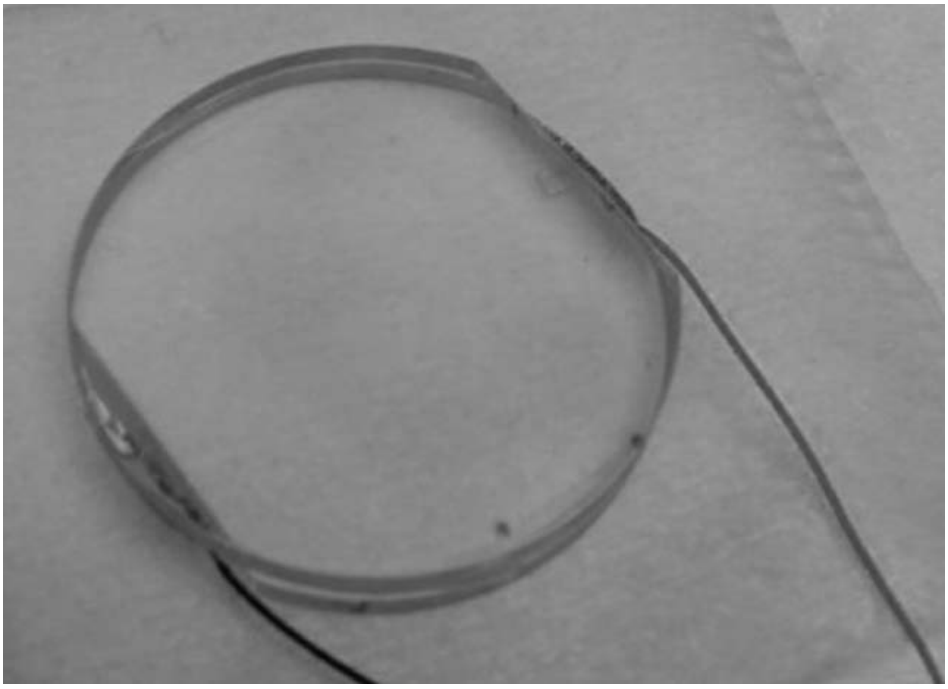

Figure 24. Image of the liquid crystal bias cell. It is composed of two sheets of optical grade glass coated with a conductive layer of gallium tin oxide. The electrodes are connected to these conductive layers, one per layer. The liquid crystal material is sandwiched between these two layers. Applying a voltage to the device creates an electric field between the electrode layers which alters the arrangement of the liquid crystal structure.

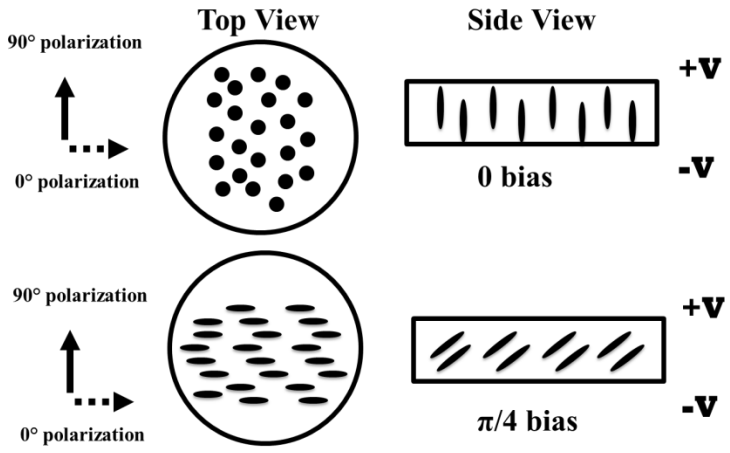

Figure 25. Diagram visualizing the operation of the liquid crystal bias cell showing a top down view (along optical path) and a side view of the device. Introduction of an electric field changes the lowest energy state of the crystalline structure and causes a reorientation of the crystals. This alters the effective surface area of the crystal that is projected into the path of the light waves. By altering this, the refractive index experienced by the separate polarizations is changed. As a result the optical path length for the two polarizations is changed and a phase bias between them is introduced.

4.2 Calibration of Liquid Crystal Bias Cell

Using an extension of the model of the DIC PSF allows for a simple technique to calibrate the bias retardation introduced by the liquid crystal bias cells. The intensity in the background of an image, acquired without a sample or in a region of the image away from the sample, is determined entirely by the bias retardation of the system. The background phase is very nearly constant because no interference is introduced by the specimen being imaged. Regions of constant background within the model defined in Section 2.4 can be described by letting $f(x, y) = 1$ which gives an equation for the intensity of any point in the background[3]

$$i_{bg}(x,y) = a\left|\iint_{-\infty}^{\infty} k(x,y)dxdy\right|^2 sin^2(\Delta\theta) \\ = a\, sin^2(\Delta\theta). \tag{16}$$

This equation is a simplification of the DIC imaging model given in Section 2.4 where the PSF model is split into the two constituent components used to define it in Eq. (1). These two components are the transmissive optics amplitude PSF $k(x,y)$ and the complex amplitude difference generated by the shear of the system which has been simplified into terms of $sin^2(\Delta\theta)$ through Euler's formula from complex analysis.

A relationship between image intensity and the bias retardation can be extracted from Eq. (16). By setting up the microscope for DIC imaging and collecting numerous images that only differ in the bias applied a correlation between that bias and the intensity can be established. Adjusting the bias is achieved by varying the applied voltage as detailed in Section 4.1. Since the device is not yet calibrated it is unknown what bias retardation is introduced for each collection, instead the result is a relation between intensity and the applied voltage. When intensity is plotted as a function of voltage, the resulting curve takes on a sinusoidal shape. This curve can then be fit to a $\sin^2$ function, as predicted by Eq.(16), to determine the relation between voltage and bias for the collected data.

A traditional DIC imaging configuration, as seen in Figure 2, was setup. The liquid crystal bias cell is introduced between the polarizer and the condenser Nomarski prism. Initially a sample is placed in the system to aid in adjusting the focus of the microscope, however it was removed before any data was collected to simplify processing of the data. The object would need to be cropped from the final data since

only the background region is of interest. The final step before gathering data is running through all possible amount of bias retardation to ensure the illumination intensity and exposure times are properly adjusted to avoid camera sensor saturation issues.

Control of the device is done through a digital control board. A 2 kHz square wave signal is applied across the device. The magnitude of the voltage applied determines the orientation of the liquid crystals in the device. This orientation in turn determines the effective refractive index of the device. As it is a birefringent material, this RI is only experienced by light polarized parallel to the crystals. Light polarized orthogonal to the crystal alignment experiences a constant RI (see description in Section 4.1 and Figure 25). With this setup was complete, images were collected across the full range of bias values possible with the liquid crystal device. The captured images were chosen by slowly adjusting the applied voltage until a slight change in intensity occurred with consideration given that the changes would be more gradual as the intensity approached its minimum and maximum. All images gathered were saved as grayscale 8-bit TIFF images.

When there is no sample in the field of view, the entire image is representative of the background and should have near constant intensity. Small perturbations are possible due to non-uniform illumination intensity, small inconsistencies in the bias cell, light scattering out of the imaging path, and light entering the system from the surrounding environment. To mitigate these factors the intensity in each gathered image is averaged to yield one representative value for each collection point. In Figure 26 these values are plotted and fit to a $\sin^2$ equation on $[0, 3\pi/2]$, the full range of bias values possible with this particular liquid crystal cell. The Curve Fitting Toolbox in MATLAB was utilized to

determine the parameters of the fit curve for the data. The end result is an equation that relates a bias value to the background intensity values. Additionally, we know what voltage was applied to create each image. Combining these two pieces of information yields a calibration curve showing the bias introduced at each applied voltage.

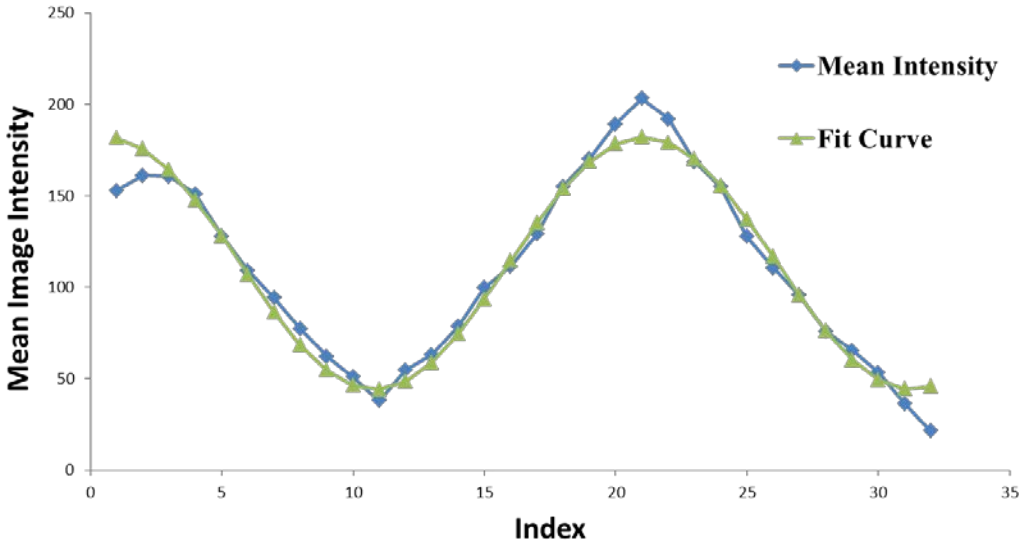

Figure 26. Plot of average image intensity for collected images to be used for calibrating the liquid crystal bias cell. Index indicates which of the 32 collected images is being displayed. Mapping these intensity values to a curve fit to Eq. (16) gives a relationship between background intensity and bias retardation. Further knowledge of which applied voltage generated a given intensity allows determination of the shear created at that voltage point.

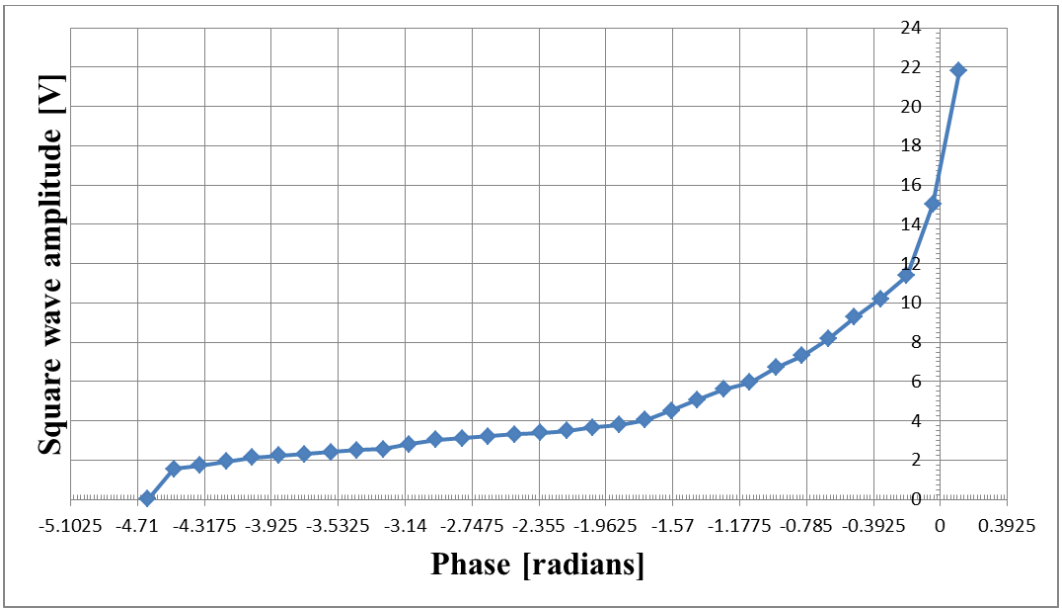

Figure 27. Final calibration curve for the liquid crystal bias cell derived from data fitting done in Figure 26. Relates applied voltage to the resulting bias retardation produced and shows non-linear response of device.

4.3 Measuring the DIC Shear of the Imaging System

Another crucial parameter of the DIC imaging model is the amount of shear distance between the coherent light waves after they are split by the Nomarski prism. One method for determining this distance is based on imaging a sub-resolved bead and measuring the distance between the high and low intensity peaks in the resulting image.[27] This technique is suboptimal as it provides an estimation of the shear that is influenced by factors other than the physical properties of the Nomarski prism itself. An improved approach based on imaging of the back focal plane (BFP) of the objective lens was investigated by Mehta and Sheppard.[28] Their approach is an investigation of the period of the interference fringes present relative to the size of the BFP.

The Nomarski prisms introduce a small variation in OPL between the two sheared light waves. In addition to shearing the light the prisms also introduce a small variation

in OPL. This variation is different for the two beams of light as they experience different refractive indices during the shearing process. This variation is ignored in DIC imaging models since any variation introduced by one prism is compensated for by the other. By removing one prism from the system this compensation is lost which results in a linearly varying OPL across the BFP of the objective lens resulting in a sinusoidal fringe profile defined by

$$P_{DIC}(\xi,\eta) = jP_{BF}(\xi,\eta)\sin(2\pi\xi\Delta - \phi)$$

$$|P_{DIC}(\xi,\eta)|^2 = |P_{BFP}(\xi,\eta)|^2\sin(2\pi\xi\Delta - \phi)^2, \quad (17)$$

where ξ and η are coordinates in the BFP (units of NA_{obj}/λ), 2Δ is the shear distance, and ϕ is the bias retardation. P_{DIC} is the resulting DIC image and P_{BF} is the bright field image. The coordinate system for each aperture is normalized to be on [-1, 1] giving the aperture a radius of 1 when express in normalized units of NA_{OBJ}/λ. The initial form of Eq. (17) is another representation of the Fourier transform of the DIC PSF given in Eq. (2).

This setup requires sample less image acquisitions resulting in a DIC image of constant background intensity (the same approach utilized in Section 4.2 to calibrate the liquid crystal bias cells). There are two important changes for this experiment. First the objective Nomarski prism is taken out in order to remove the bias compensation effect described above. Second, the imaging path is altered to change the focal plane imaged by the camera sensor. Rather than the object's imaging plane being projected on to the camera sensor, the back focal plane is projected on to the sensor. This, results in an image of the Fourier transform of the optical system being captured. It takes on the

appearance of a constant value modulated by a sinusoidal signal, a fringe pattern, and is a physical manifestation of the DIC PSF model developed in Section 2.2.

Since the shear distance is a constant, unchanging value determined by the physical characteristics of the Nomarski prisms, the bias retardation is the only alterable parameter of the system. The work in Section 4.2 to calibrate the bias cells allows this parameter to be adjusted in an accurate and systematic fashion. As the bias is increased the fringe pattern shifts across the field of view as shown in Figure 28. Capturing these patterns and combining them into one continuous allows for the frequency of the sinusoidal pattern to be computed. The end result is an accurate measurement of the shear distance of the DIC system.

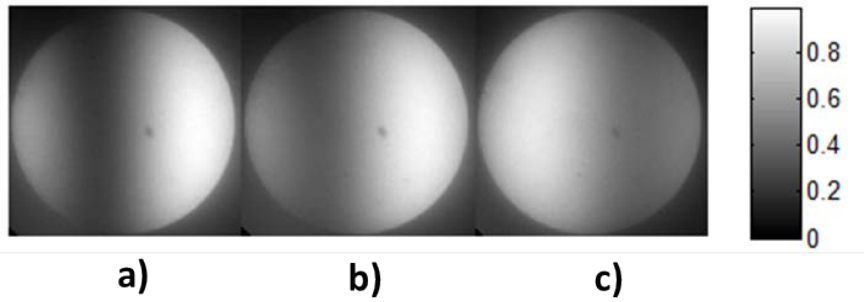

Figure 28. Demonstration of the shift in fringe patterns in images of the back focal plane of the objective lens that result from changing the bias retardation of the imaging system. Shown are fringe patterns for bias retardations of a) $3\pi/16$, b) $3\pi/8$, and c) $3\pi/4$, respectively, imaged using a 10x/0.3NA objective lens with 540 nm illumination.

The collection of data for this analysis is straightforward. First the bias must be swept across all values to be introduced during the collection process and careful attention paid to the minimum and maximum intensity created. The intensity of the images will vary with change in bias and it is crucial that the illumination strength and

exposure time be adjusted to properly capture the dimmest images and to avoid saturation on the brightest images. This is the same precaution taken when calibrating the bias cell as described in Section 4.2. Bias retardations from 0 to $3\pi/2$ radians in increments of $\pi/12$ were applied and an image collected of each resulting fringe profile.

The images acquired in this manner require some processing before a final determination of the shear distance can be made. Due to the alignment of the polarizer, analyzer, and Nomarski prisms in our microscope, the shear directions are along a diagonal axis at a 45 degree with respect to the horizontal axis. Additionally, the region of interest does not fill the entire field of view of the camera sensor. To simplify extraction of a profile, the images are first rotated to align the shear with the horizontal axis. They cropped to remove all background information introduced due to the fringe profile occupying a small region of the camera field of view. Non-uniform illumination also causes the fringe profiles to exhibit slight variations along the axis orthogonal to the shear direction. To mitigate this anomaly, profiles are created by computing an average of the central region of the fringe pattern rather than just plotting intensity along a single line through the center. Some example corrected images can be seen in Figure 28 and the resulting profiles are shown below in Figure 29. The profiles are normalized as a group to have intensity values in [0, 1] to simplify the curve fitting process in later steps. Additionally, the coordinate system of each profile is normalized such that the entire aperture is defined on a support of [-1, 1].

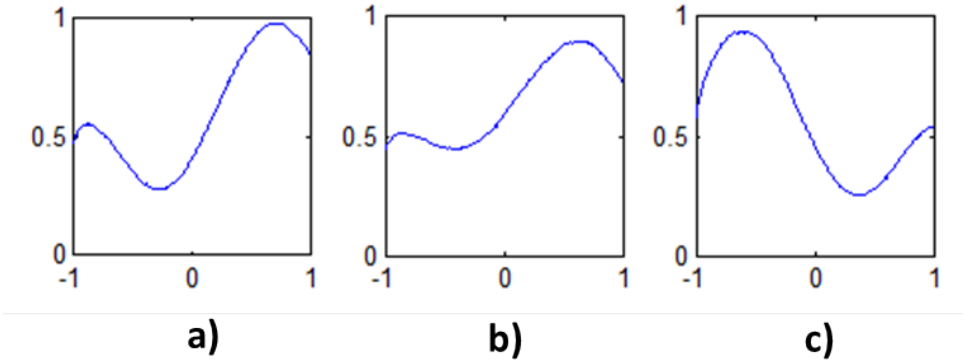

Figure 29. Central profiles through the fringe patterns shown in Figure 28 at bias retardations of a) 3π/16, b) 3π/8, and c) 3π/4 imaged using a 10x/0.3 NA objective lens.

After extracting profiles through each fringe pattern, they must be stitched together to create one continuous representation that can be fit to Eq. (17). This process involves manual alignment of the individual fringe profiles to best create the overall sinusoidal pattern of the modulation. While creating a longer fringe pattern results in a more accurate determination of the shear than would be possible using a single profile, the process of combining the series of data does introduce a potential source of error. The is because the profiles do not align perfectly as shown in Figure 30; however the final result after combining the profiles produces a reasonable approximation of a sinusoid as shown in Figure 30. Computing a curve fit, an example of which is shown in Figure 31, of Eq. (17) to this data yields a final determination of the shear for a given lens.

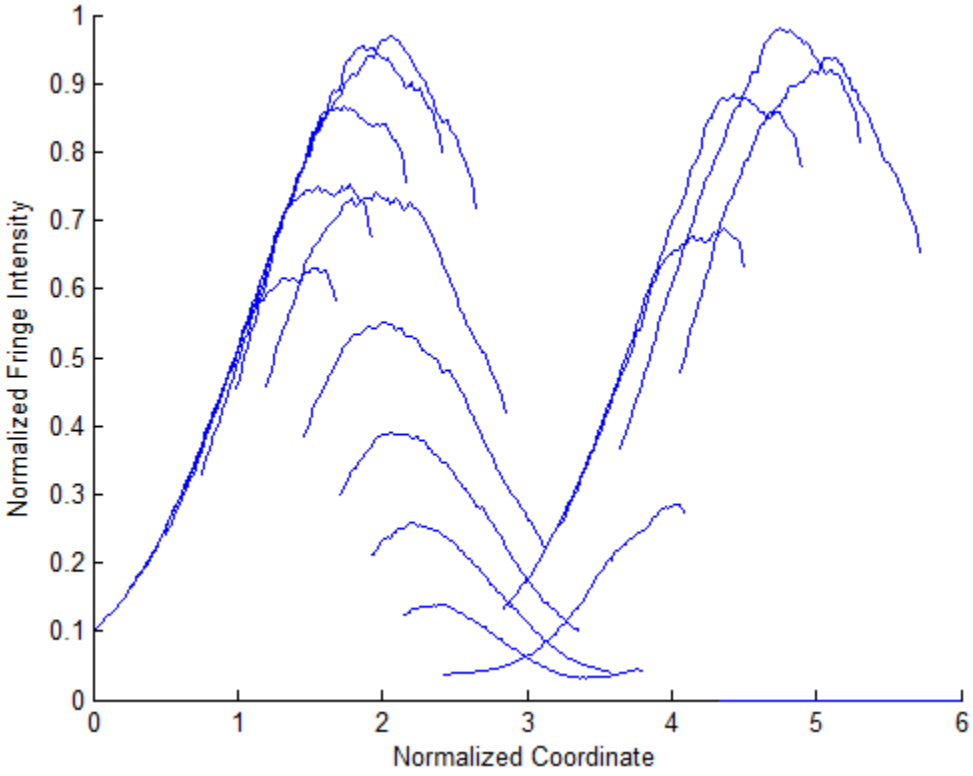

Figure 30. Fringe profile data collected to determine shear of Nomarski prisms when using a 63x/1.4NA lens. Data was collected for bias values from 0 to $3\pi/2$ radians in increments of $\pi/12$ radians. Each line segment represents a fringe profile for a different bias retardations' fringe profile. The coordinate system for each profile (individual line segment) has been normalized to [-1, 1] as described previously. The final stitched profile extends beyond the aperture in order to capture the shifting phenomenon resulting in a large coordinate system for the final profile.

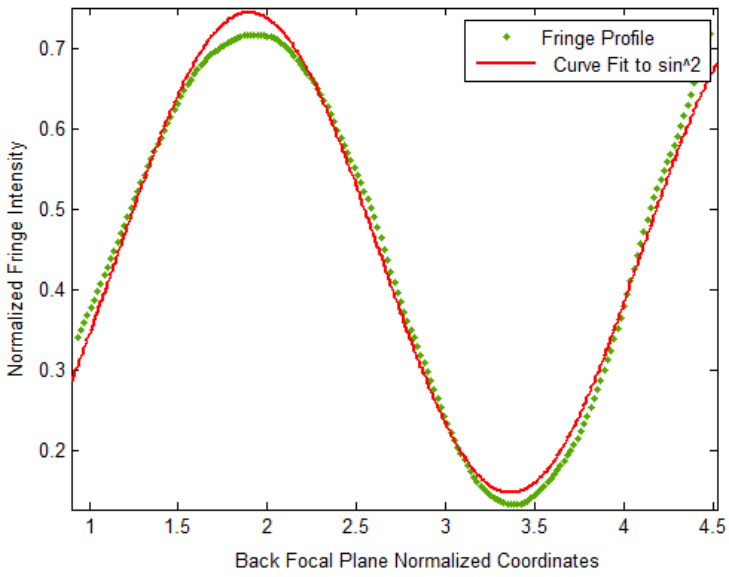

Figure 31. Fringe profiles from Figure 30 averaged together to form a single profile. Fitting Eq. (17) to this profile yields the shear distance of the system.

Processing data for the 63x/1.4 NA lens in this fashion yielded a shear distance measurement of 0.17 µm. The shear distance for the 10x/0.3 NA lens was determined to be 0.257 µm. The Rayleigh criterion sets a theoretical upper bound on the shear distance of $2\Delta < 0.61\lambda/NA_{OBJ}$. For the 63x/1.4 NA lens this equation yields a maximum shear distance of 0.2353 µm, and for the 10x/0.3NA lens a maximum shear of 1.098 µm. The final determined shear values are well within these bounds.

4.4 Experimental Data Acquisition

Proper microscope setup for DIC imaging is a straightforward process and can be achieve with very little modification to most bright field microscopes. This is one of the reasons DIC has become a popular imaging modality for phase imaging. A diagram of the system is shown in Figure 2 laying out the components needed and their positioning in the microscope. After the initial installation and calibration of the polarizers and

Nomarski prisms, it is trivial to modify the microscope to change between imaging modalities. The main components of our microscope are shown in Figure 32. Not explicitly labeled in this image are the condenser prism and the DIC bias cell. The condenser housing contains a rotating tray which allows for the selection of various optical components designed to fit inside the tray's compartments. The condenser prism is located inside one of these trays and can be moved into and out of the system easily. The bias cell rests on the frame holding the polarizer at the bottom.

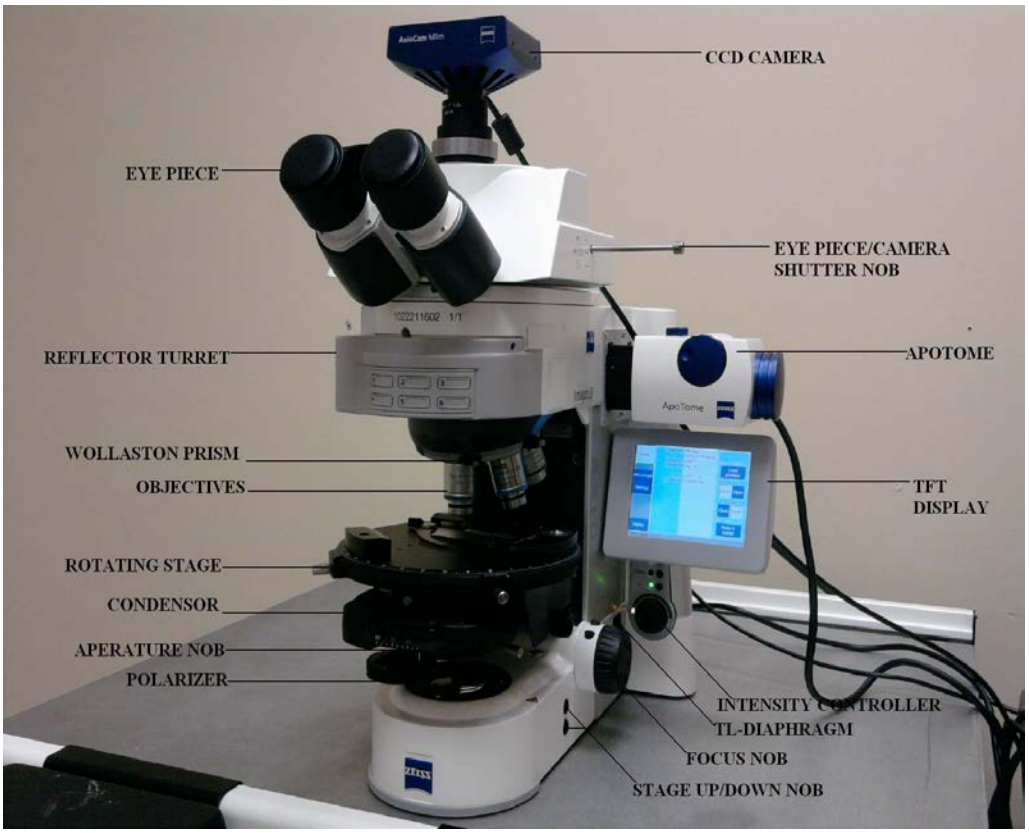

Figure 32. Overview of the main components of the Zeiss AxioImager Z2 utilized in the Computational Imaging Research Laboratory.

Once the hardware is configured for DIC imaging, some further adjustments are necessary to ensure the quality of the images gathered is acceptable. A narrowband light filter with mean wavelength 540 nm is used. This is done to match the imaging model utilized for this algorithm which was developed with the assumption that monochromatic illumination is used. The primary system adjustment involves getting the object in good focus and changing the illumination intensity and camera exposure settings to create a strong, low noise signal while also avoiding saturation of the sensor. This step is done

with the bias cell in place and adjusted such that the image contains a desired level of contrast. There may be some iterative adjustments between these parameters as altering one can affect the others and a balance must be achieved.

Collection of just DIC data at this point is very straight forward once the above setup and adjustments are completed. Our methodology only requires two collections to be made at orthogonal shear directions. This is accomplished by rotating the sample stage by 90 degree between collections. Before collecting either image it is important to rotate the stage to ensure the sample stays within the field of view and does not end up too close to the edge of the image. One additional step to this process was recently included to assist in the registration of the two rotated images. This registration process involves the use of bright field images gathered at each sample rotation. Since bright field is not a rotationally sensitive image methodology, it greatly reduces the complications of performing images registration. Obtaining all the required data simply involves taking a DIC image, removing the Nomarski prisms from the system, taking a bright field image, rotating the stage, taking a second bright field image at the new orientation, replacing the prisms, and collecting the final DIC image. Performing the collections in this order minimize the opportunities for disturbing the sample and altering the focus or moving the object. The floating optical table on which the microscope is mounted also serves to reduce these disturbances.

4.5 Preprocessing Experimental Data

Proper registration of rotationally diverse images is vital for the performance of the AM algorithm. The underlying object properties being estimated at a given point are based upon conflicting information if the images are not properly registered. In image regions that are largely uniform this is not an issue, but for portions showing fine object detail the impact can be significant. It is easiest to demonstrate this issue using simulated data where complete control of the process is possible. Doing so allows for a comparison of the estimations when using perfectly registered images to those of varying amounts of error in registration while being able to reference this all back to the known true numerical object function as seen in Figure 33.

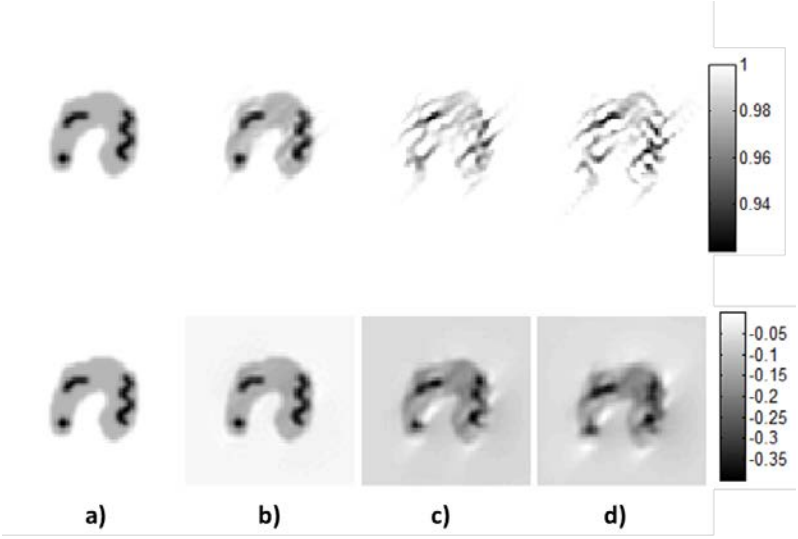

Figure 33. Study of the effects of poor registration on the performance of the AM algorithm completed using a simulated numerical blob object, no noise, and no roughness penalty. Top row shows object magnitude, bottom row shows object phase. Columns represent a) the true simulated numerical object, b) estimations performed with perfectly registered data, c) estimations performed with data misregistered by a shift of one pixel horizontally and one pixel vertically, and d) estimations performed with data misregistered by a shift of three pixels vertically. Generated using 10x/0.3 NA lens, shear 0.34 μm, sampling 0.34 μm, bias $\pi/2$, and 540-nm illumination.

Achieving perfect registration of experimentally collected data is a major challenge. One technique that assists in registration of images is the use of fiducial marks; however they suffer from the same issues as using the object data itself: when viewed under differing shear directions the object takes on a different appearance. Even symmetrical objects like the simulated and experimental bead objects are difficult to register. While they look the same, the alignment and shape of the shadowing contrast in the images have no easily and directly correlated features. Additional data collection is required to circumvent this problem as outlined in Section 4.3 which describes the microscope setup and data collection procedures. The bright field images gathered at each rotation is used for the following phase registration technique.

Since the data gathered during bright field microscopy is not rotationally dependent it can be used for registration purposes. Any shift required to align the bright field images can then be applied to the DIC images resulting in proper registration. The use of fiducial marks for registering these images is difficult because they have to be both in the field of view of the object being imaged and at the same depth as the image to ensure they are in good focus. Instead and approach based on analysis of the Fourier transforms of the two images has been implemented. It takes advantage of the Fourier transform property that any spatial translation of an object results in an equal amount of phase shift in its frequency domain representation.

This approach works by computing the Fourier transform of both images and extracting the phase information for each. One phase mask is subtracted from the other resulting in a map of the differences in phase content. This phase difference is used to create a complex valued phase mask. Finally this phase mask is Inverse Fourier

transformed resulting in a collection of impulse values that can be interpreted as a correlation map between the two images. The location with the strongest correlation, indicated by the highest value in the result, indicates the amount of shift between the two images. When tested with simulated images of a simple shape this technique provides accurate results with no ambiguity on the shift amount needed as can be seen in Figure 34. When used on experimental data, which suffers from low signal content due to the weak absorption properties of the sample, the results can be more difficult to interpret as seen in Figure 35.

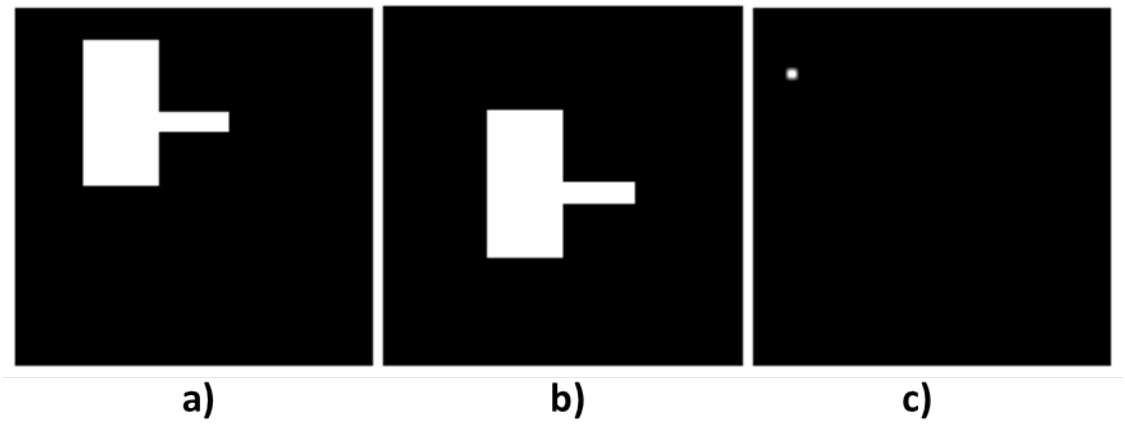

Figure 34. Example of phase registration results on a simulated image to validate approach before trying with experimental data. Images shown are a) original test object, b) test object shifted along both axes, and c) resulting correlation map from the phase registration technique. The pixel location of the single impulse indicates the amount of shift between the two images.

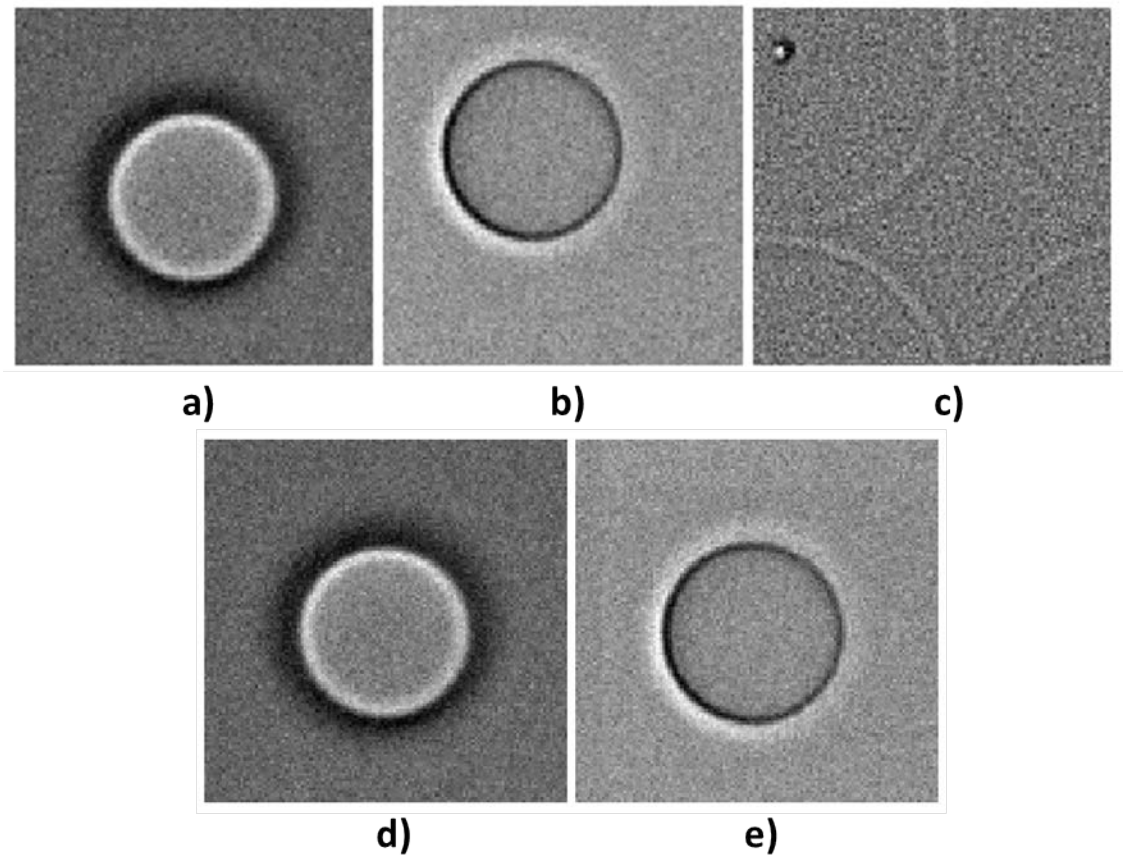

Figure 35. Phase registration results applied to experimental bright field images of polystyrene beads. Shown are a-b) cropped portion of experimental bead images for both shear directions, c) correlation map from phase registration technique, d) first image in same location, e) second bead image cropped again with region of interest shifted by amount dictated by the correlation map in c). Compared to Figure 34, the correlation map for this data set has a range of potential shift amounts demonstrating the difficulty of applying this approach to images with low signal content.

The second preprocessing step serves to correct the intensity levels of the forward model DIC images used to evaluate the estimation performance. The development of the forward imaging model in Eq. (4) includes an attenuation parameter *a* to adjust for illumination intensity. An ideal system, which exists only in simulation, will experience full strength illumination at every step of the image formation process. In real application, however, some light is lost resulting in a reduction of intensity. This loss occurs do to adjustments to the condenser aperture size necessary to increase illumination coherence, attenuation caused by the polarizer and analyzer, light scattering at various stages of the system, and inefficiencies in the camera sensor. As a result of this, the forward model applied to a given numerical object will produce higher intensity synthetic images than a real object with exactly equivalent optical properties.

An attenuation constant must be computed to correct for this discrepancy. This is mostly easily done by analyzing the background region of an image. This area is of constant magnitude making it easy to work with and additionally it can be represented by a numerical object value of 1 as seen previously in the development of the bias calibration methodology discussed in Section 4.2. The goal is to find a constant scale factor to adjust the background intensity of the forward model data to that of the experimental data. Given that there are slight variations across the image it is necessary to find a value that best corrects these values across the background region as a whole. This is done through computing the inner product of the experimental and forward model data and dividing by the norm of the forward model data. This requires that the

algorithm first be run with the parameter a_k set to 1 in order to generate the data necessary to determine a proper value. These results can be seen in Figure 36 and Figure 37.

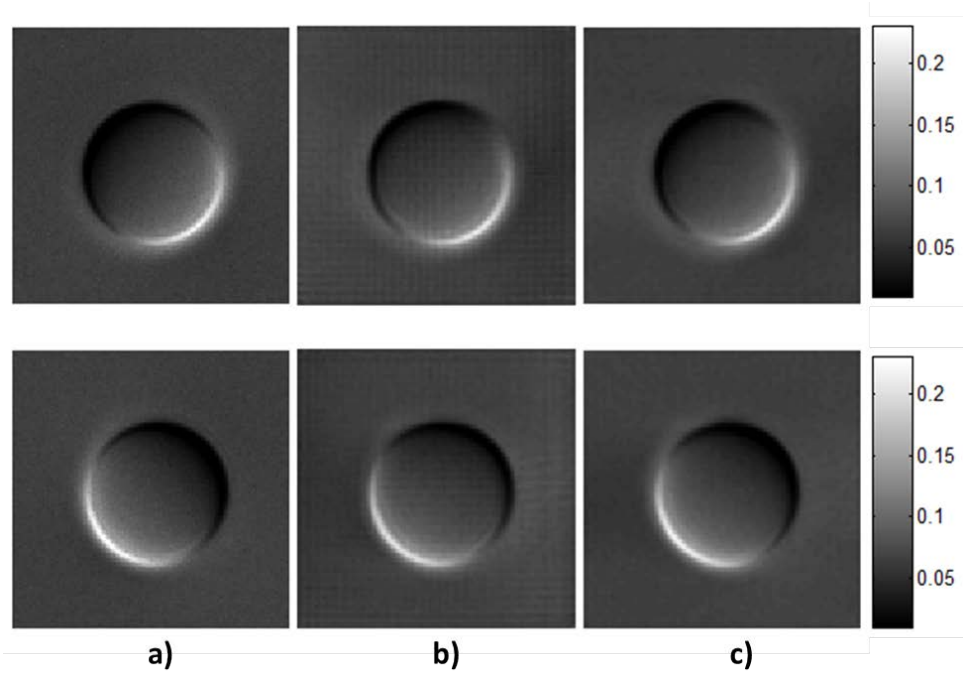

Figure 36. Effect of proper selection of attenuation constant *a* from Eq. (5) on performance of AM algorithm's final forward model image results. Each row shows a separate shear direction, top is sheared along 315 degrees, bottom sheared along 45 degrees. Columns show a) experimentally gathered DIC images of 6 µm ring beads, b) forward model applied to final object estimation when $a_0 = a_1 = 1$, and c) forward model applied to final object estimation when $a_0 = 0.9078$ and $a_1 = 0.8849$. Generated using 63x/1.4 NA lens, 0.17 µm shear, 0.1 µm sampling, and $\pi/4$ bias at 540 nm illumination

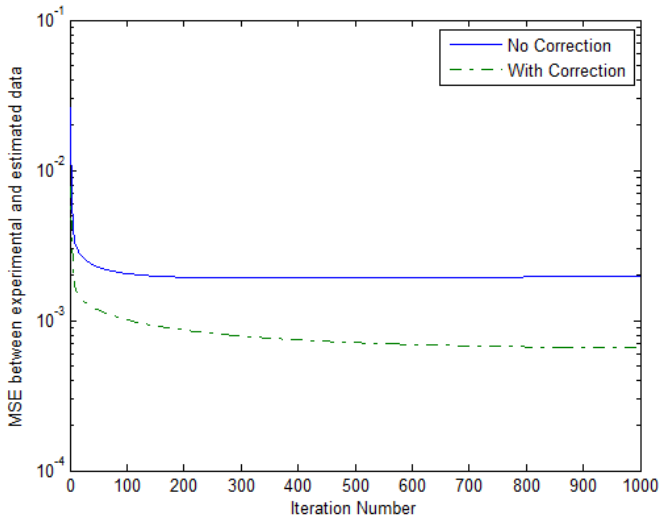

Figure 37. Error curves for results shown in Figure 36.

4.6 Results from Applying AMA to Experimental Data

One of the primary goals of the research done for this thesis was applying the AM algorithm to experimentally gathered data and validating the accuracy of these results. This is accomplished in two ways. First, we used a simple physical object, polystyrene fluorescence beads, and imaged them experimentally. This data, along with knowledge about the physical composition of the object, was then used to inform the creation of a numerical simulation of the beads as developed in Section 3.2. Doing so allows a validation of the results from experiment, where we do not know the true object, with those from simulation. Lastly, we can compare the algorithm's output to that of another established quantitative phase imaging technique. In this case we utilized images of yeast cells and the results of applying the Spiral Phase Integration technique to the results obtained with our algorithm.

Looking first at the bead data, it is necessary to first validate the numerical object model and forward imaging results. While the simulation results will never perfectly mirror experimental results due to the simplified nature of our model, a reasonably close approximation is important. As can be seen in Figure 38, the forward model comes close to the experimental data. The edges of the bead along the shear directions both take on a crescent shaped intensity profile demarcating the edge of the bead. The images also both have a bas-relief appearance.

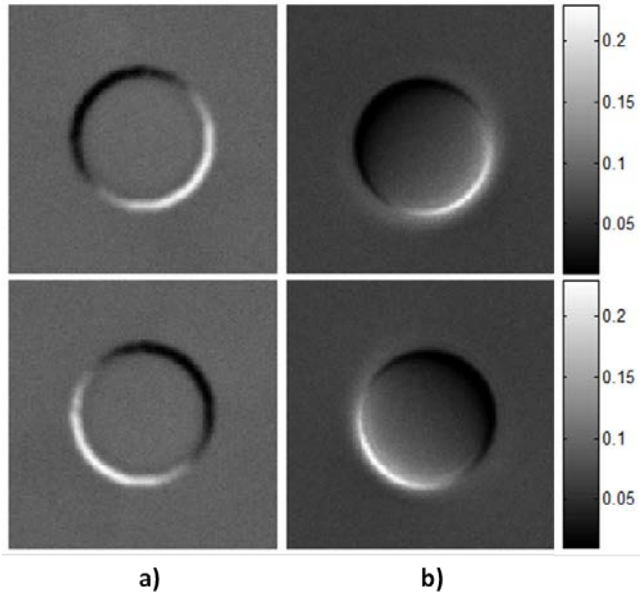

Figure 38. Comparison of a) numerical bead object passed through forward model in Eq. (5) and b) experimental ring bead images. Top row shows images with shear direction of 135 degrees, bottom row shear direction of 45 degrees. Forward model computed using DIC PSF representing 63x/1.4 NA lens at 0.17 μm shear, 0.1 μm sampling, bias of $\pi/4$, and illumination of 540 nm. Experimental data collected using lens and system with same parameters.

After establishing an acceptable numerical object to simulate the bead, it is possible to compare the estimations returned by the AM algorithm for each. Since the experimental data is subject to a small level of noise, it is important to utilize the noise study from Section 3.4 to determine an appropriate penalty value. The simulated dataset must also be corrupted by an equivalent noise level to ensure both datasets match as well as possible. The standard deviation of background intensity was chosen as a metric for comparing the noise corruption in each image. The standard deviation of the experimental images was determined to be 0.0065. A new simulated bead dataset was created and a Gaussian noise mask with standard deviation 0.0065 was applied. The reported SNR for this data was 42.8 dB and based on the penalty study done in Section 3.4 a penalty weight of $\kappa = 0.005$ was chosen. The only metric available to quantify performance of the algorithm on experimental data is the MSE between the experimental DIC images and the forward model synthetic images based on the object estimations as shown in Figure 40.

.

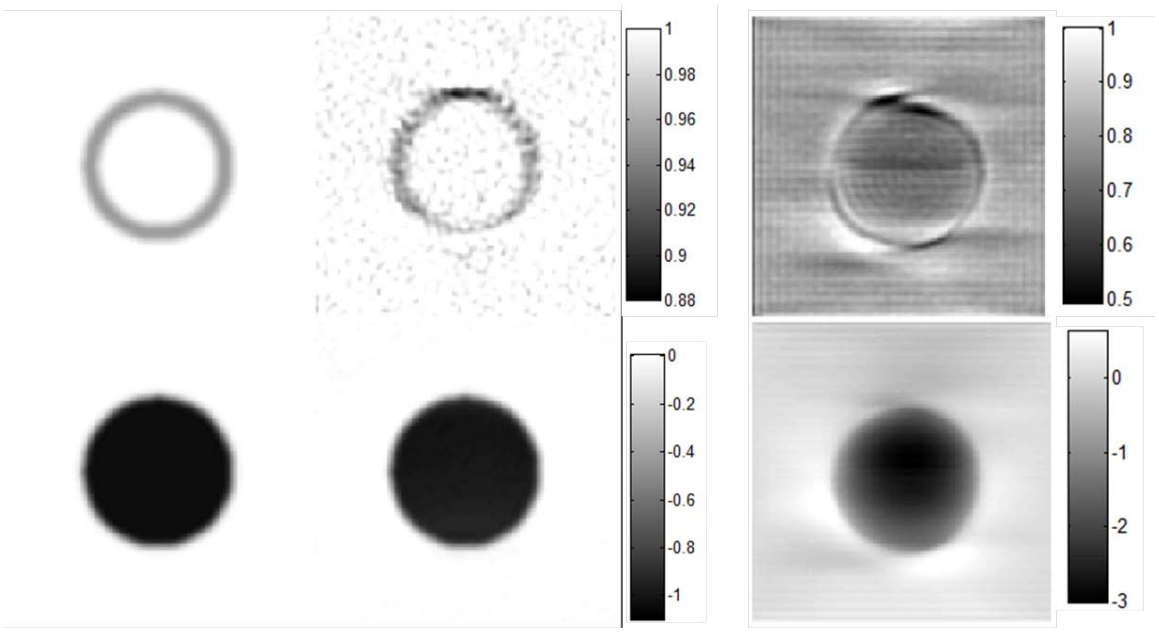

Figure 39. AM algorithm object estimations for 6 µm polystyrene bead data: a) true numerical simulated object, b) AM estimation of object from simulated forward model images at 30 dB SNR, and c) AM estimation of object from experimental data. Top row shows magnitude of complex valued object function, bottom row shows phase. Forward model computed using DIC PSF representing 63x/1.4 NA lens at 0.17 µm shear, 0.1 µm sampling, bias of $\pi/4$, and illumination of 540 nm. Experimental data collected using lens and system with same parameters. Results shown for 5,000 iterations and using parameters $\alpha = 0.45$, $\beta = 1$, and γ computed using Eq. (15) and $\kappa = 0.005$.

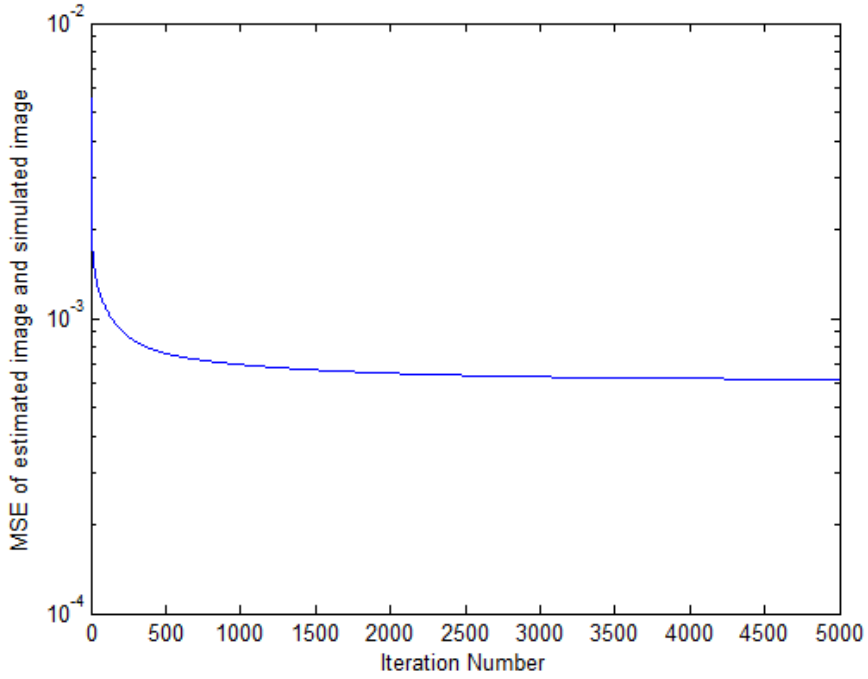

Figure 40. MSE between experimental DIC images of 6 µm polystyrene ring bead and synthetic forward model DIC images based on AM algorithm object estimation.

The next step is processing experimental yeast data. The setup is exactly the same as processing the experimental bead data. Given that the image is degraded by noise, we again compute the standard deviation of the background intensity to help with the selection of a value of κ. For this image set the background intensity standard deviation was found to be 0.0095. This time a simulated blob dataset was generated as it is a better approximation of the yeast cells than the bead would be. This produced a SNR of 39.6 dB which still suggests $\kappa = 0.005$. Results of running AM with this κ value are shown in Figures 41 and 42. The results show significant artifacts and demonstrate another important property of the roughness penalty: removing the influence of the null space on the inverse system model. This helps reduce the artifacts and noise introduced when invalid updates are created in the estimation process. By increasing κ to 0.25 the

artifacts are significantly reduced at the expense of a slightly smoother object resulting in a final forward model image that is also smoothed as seen in Figure 43 and Figure 44. The error curves for these two runs are shown in Figure 45 and demonstrate an improvement to the final image estimate justifying the tradeoff between noise mitigation and object over smoothing.

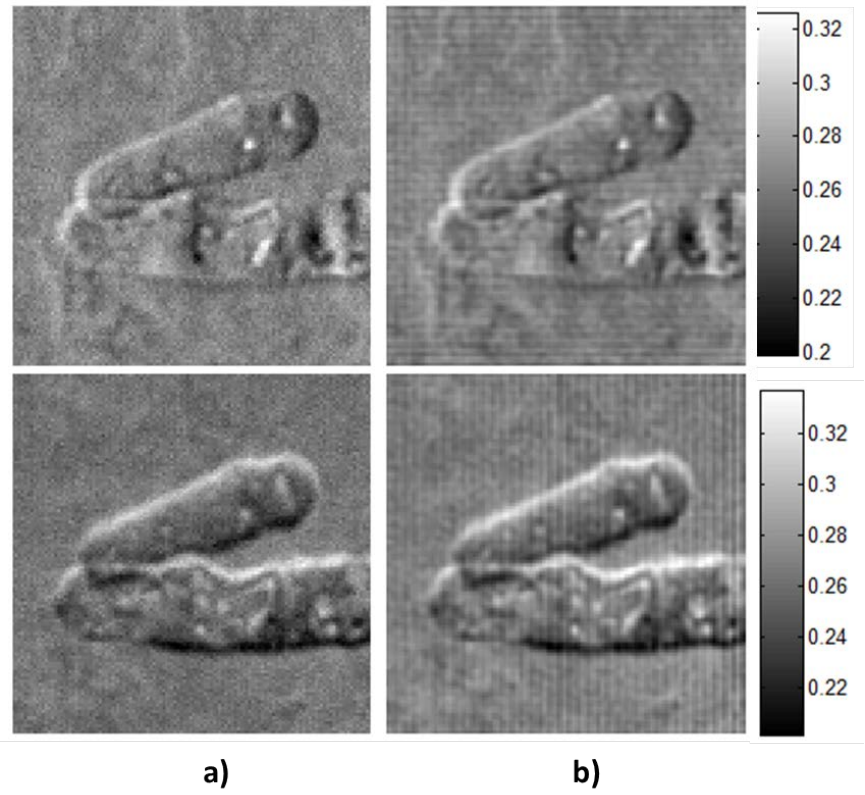

Figure 41. Results showing a) experimental yeast data and b) forward model of final object estimates from AM algorithm computed suing $\kappa = 0.005$. Top row shows images with shear direction of 0 degrees, bottom row shear direction of 270 degrees. Forward model computed using DIC PSF representing 63x/1.4 NA lens at 0.24 µm shear, 0.12 µm sampling, bias of $3\pi/2$, and illumination of 540 nm.

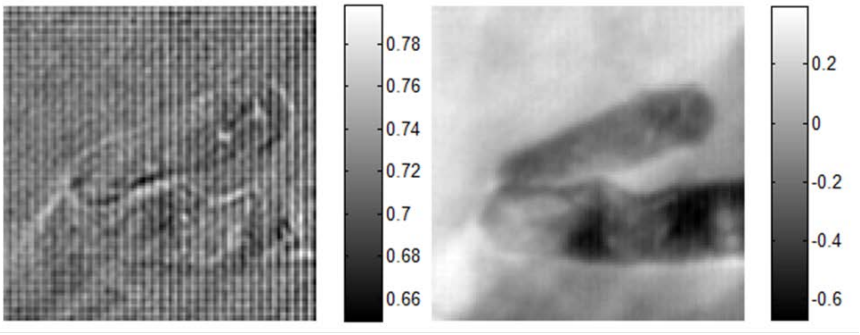

Figure 42. Object function estimation from AM algorithm based on experimental data in Figure 41-a which result in the forward model images in Figure 41-b showing a) object magnitude and b) object phase. Presence of strong artifacting in magnitude estimation indicates improper roughness parameter selection. Use of too weak of a parameter allows undesired, and detrimental, high frequency content to be included in inverse imaging model. Generated using DIC PSF representing 63x/1.4 NA lens at 0.24 μm shear, 0.12 μm sampling, bias of $3\pi/2$, and illumination of 540 nm. AMA was run for 5,000 iterations using $\alpha = 0.45$, $\beta = 1$, and γ computed using Eq. (15).

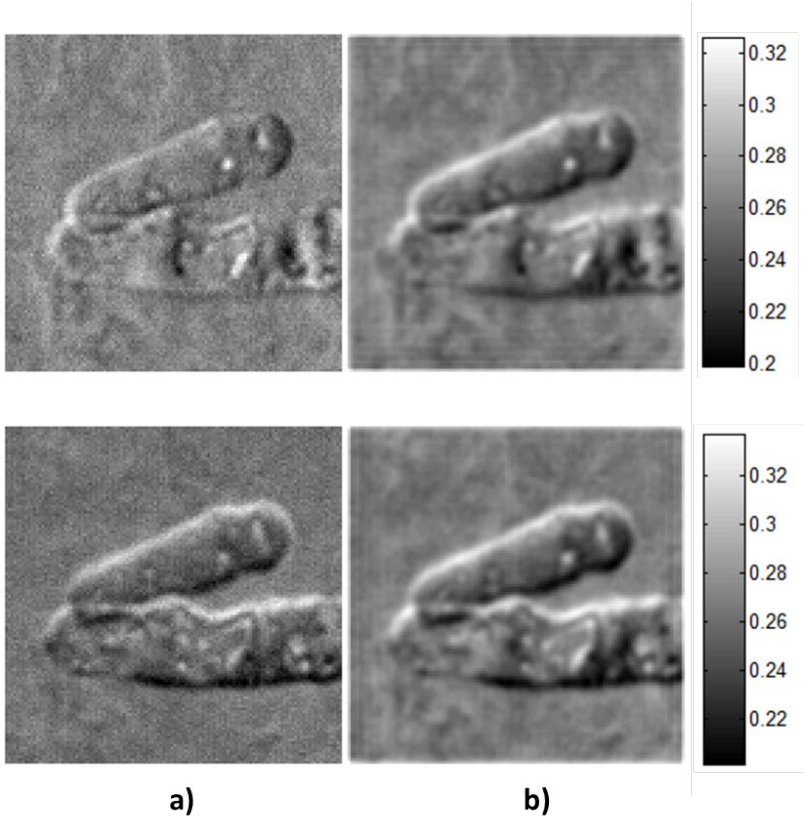

Figure 43. Adjusting value of κ to 0.25 results in improved performance over estimations using κ = 0.005 shown in Figure 44. The stronger roughness penalty discourages the high frequency content of the estimations which resulted in the previously seen artifacting. Comparison of a) experimental yeast data and b) forward model of final object estimates from AM algorithm. Top row shows images with shear direction of 0 degrees, bottom row shear direction of 270 degrees. Forward model computed using DIC PSF representing 63x/1.4 NA lens at 0.24 μm shear, 0.12 μm sampling, bias of 3π/2, and illumination of 540 nm.

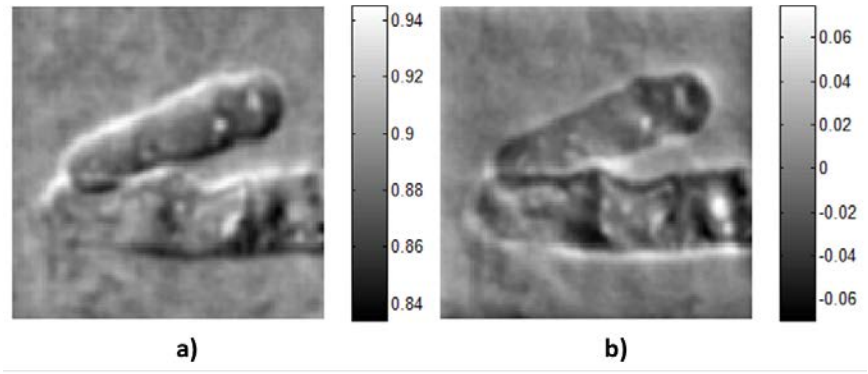

Figure 44. Object function estimation from AM algorithm based on experimental data in Figure 43-a which result in the forward model images in Figure 43-b showing a) object magnitude and b) object phase. Not improved qualitative appearance of magnitude estimation. Generated using DIC PSF representing 63x/1.4 NA lens at 0.24 μm shear, 0.12 μm sampling, bias of $3\pi/2$, and illumination of 540 nm. AMA was run for 5,000 iterations using $\alpha = 0.45$, $\beta = 1$, and γ computed using Eq. (15).

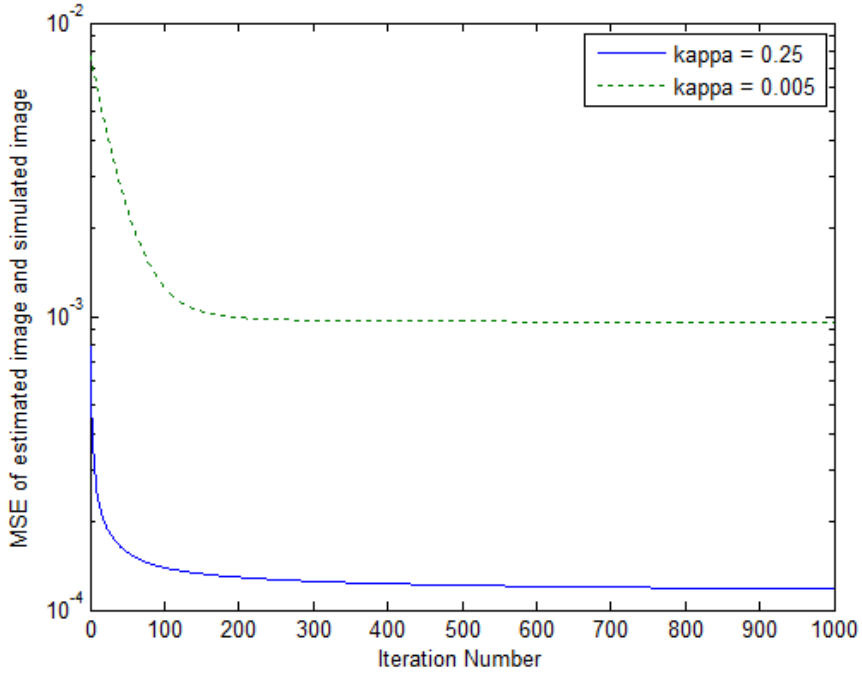

Figure 45. MSE between experimental image and forward model image of the object estimated from the yeast data using the AMA and two difference values of κ: $\kappa = 0.005$ and $\kappa = 0.25$ associated with the data in Figure 41 and Figure 43.

4.7 Comparison of AMA and SPI Results

The lack of simulated results to verify the yeast estimations is problematic. Trusting the results is made possible through the validation done using the bead object; however a comparison to another quantitative phase imaging approach is desired. Spiral Phase Integration[1, 2] is another technique that can fulfill this need. SPI provides information only about the phase of the object, but this is sufficient for validating the phase estimation results of the AM algorithm. It is also important to note that SPI does not return an exact value for the phase mask, but rather it turns a set of non-linear anisotropic phase contrast images into a linear isotropic mapping of phase values.[2]

SPI functions by taking eight phase-shifted DIC images of an object. Images are collected along two orthogonal shear directions and at four bias retardations, 0, $\pi/2$, π, and $3\pi/2$. The four images for each shear direction are phase shifted to yield a phase gradient for that collection[29] and then combined using a spiral phase integration technique to yield a final isotropic linear phase mask for the object. A comparison of SPI to AM utilizing experimental bead data is included in Figure 46 for the sake of thoroughness. Results of applying SPI to the yeast data set are shown in Figure 47.

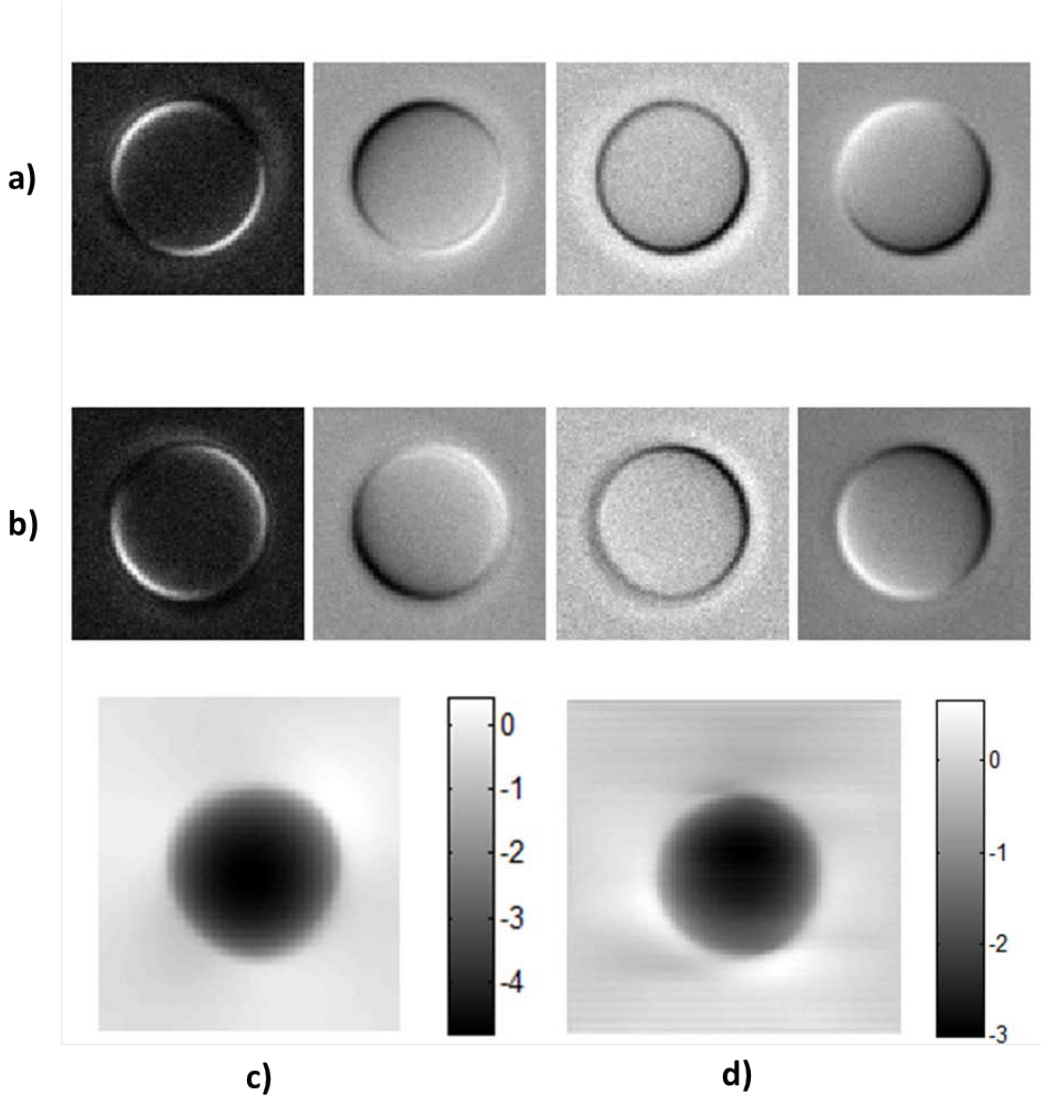

Figure 46. Comparison of bead phase estimations computed with the SPI (c) and AM (d) algorithm. Shown: rows a & b) phase shifted images along shear direction of 45 degrees and 135 degrees, respectively, and from left to right: bias retardations of 0, π, π/2, 3π/2, c) SPI results showing linear isotropic estimation of phase (unit less), and d) AMA results showing phase mask in radians. Note inversion of dark and light regions between 1st and 3rd as well as 2nd and 4th images in (a & b). This is a result of the bias retardation shifting the wave fronts by half a cycle causing locations of constructive and destructive interference to swap.

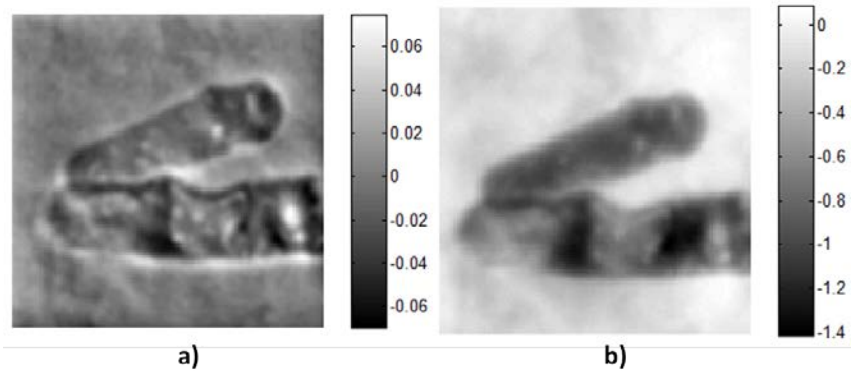

Figure 47. Phase estimation results of a) AM algorithm (shown in radians) and b) SPI algorithm (unit less measurement) on yeast cell data showing similarity of final results. Both show linear isotropic phase of underlying object, however according to theory SPI is skewed by some additional unknown linear mapping.

The results of processing the bead data support the existence of some linear transformation between the SPI results and those generated by the AM algorithm. It is known that the bead has a near uniform phase function shifted relative to some uniform background. This is mirrored by the SPI result which appears to be more blurred than the AM result. The results for the yeast data show similar structure between the phase estimations, but contain a few differences. Most notably the SPI results have less structure and fine detail and appear as a smoothed version of the AM results. There is also a difference in the relative distribution of values between the two. AM yields a background relatively close to zero with both positive and negative phase estimates for differing regions of the object. In SPI, the background is again zero, however the phase function provided is entirely negative valued.

CHAPTER 5

SUMMARY AND FUTURE WORK

5.1 PSF Model Implementation

Proper computation of the DIC PSF is a key to achieving the best results when working with any computational imaging research. The PSF forms the basis from which the rest of the model is built. The DIC PSF model has been developed and validated through numerous other publications (Section 2.2). This thesis has presented two key improvements, better sampling and rotation, for the implementation of that model within the computational framework utilized for this algorithm. This was accomplished by moving the resampling and rotation of the PSF data from the spatial domain into the Fourier domain (Section 3.1).

This can best be viewed through the final forward model output when estimating the object function of experimental polystyrene bead images. Since the bead images were created using the true physical PSF of the microscope system they are well suited for verifying the model being utilized. Additionally, since the beads are simple structures, any deviations from the expected results are easy to identify. Figure 48 demonstrates the effects this can have on final results. The algorithm was run twice with the exact same parameters while changing the PSFs utilized to be those shown in Figure 7. Using the poorly rotated version produced streaking and wave-like artifacts in the forward model estimations. This causes the underlying object estimates to become equally distorted due to the updates for each iteration being based upon substandard model outputs.

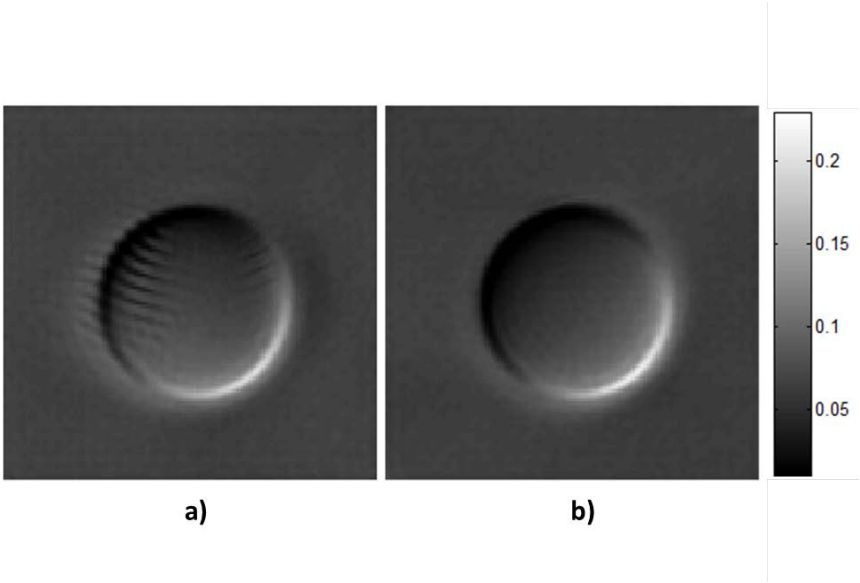

Figure 48. Comparison of forward model synthetic DIC images using different PSF model implementations as shown in Figure 7. Shown are a) results using the previous implementation with inferior rotational approximations and b) an improved approach that yields properly sampled PSFs when rotated. Both PSFs represent a 63x/1.4 NA objective lens with bias $\pi/4$, shear 0.17 μm, sampling 0.1 μm, and illumination of 540 nm

5.2 Estimations of Simulated Data

The use of simulated data plays a key role in the development of any computational imaging model. Having full system knowledge simplifies the testing of models and allows a greater level of insight to issues that arise and potential changes that can be made to remediate them. The creation of a numerical bead object (Section 3.2) to assist with validation of experimental results was completed and showed promising estimation values as shown in Figure 39.

The algorithm utilized a set of parameters to govern the behavior of the object estimation updates. Selection of these parameters has a large influence on the quality of the final result. In looking at the performance of the algorithm using two alternative sets of parameters on noiseless data, the newly derived equations were determined to

outperform the previous implementation. This can be seen when looking at results from a noiseless simulated blob estimation and is verified through a reduction in the MSE of both the magnitude and phase of the estimated object.

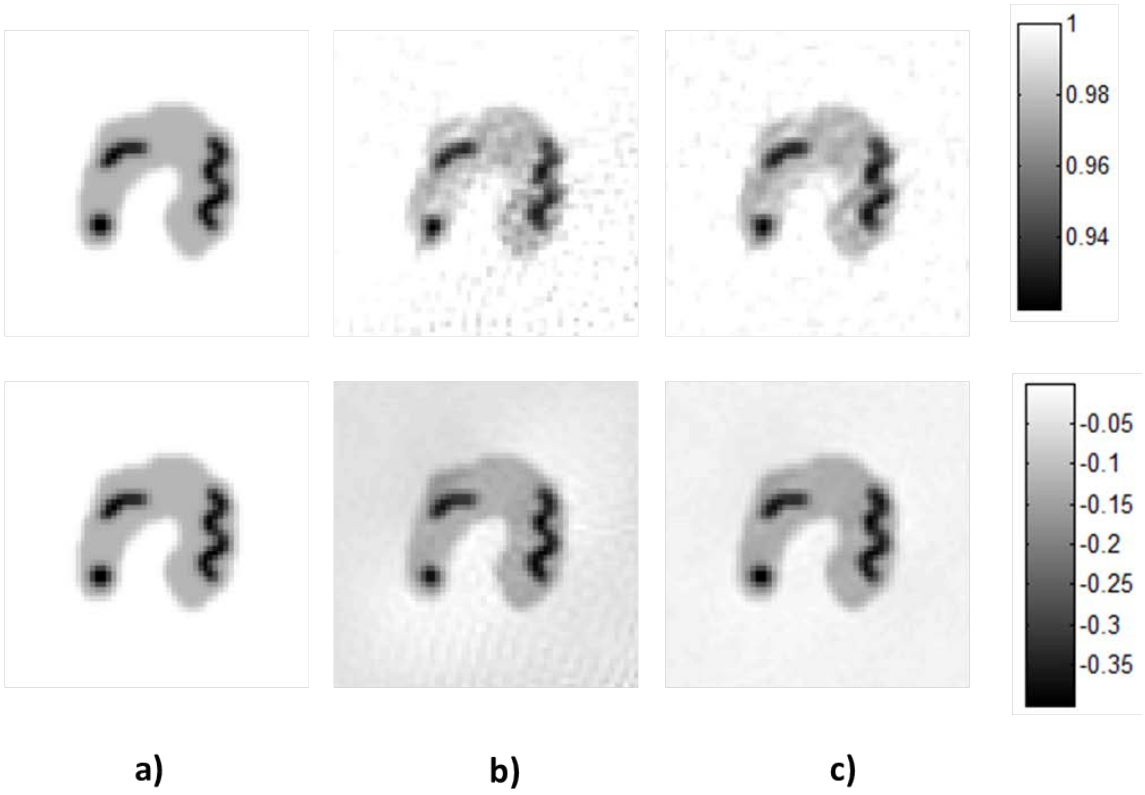

Figure 49. Estimation of numerical blob object using two sets of parameter equations, shown are: a) true object function, b) original iterative computation of parameters and b) new simplified analytic equations for algorithm parameters. Top row: object function magnitude. Bottom row: object function phase. Generated using 10x/0.3 NA lens, shear 0.34 μm, sampling 0.34 μm, bias $\pi/2$, and 540 nm illumination using $\alpha = 0.45$, $\beta = 1$, and γ computed using Eq. (15).

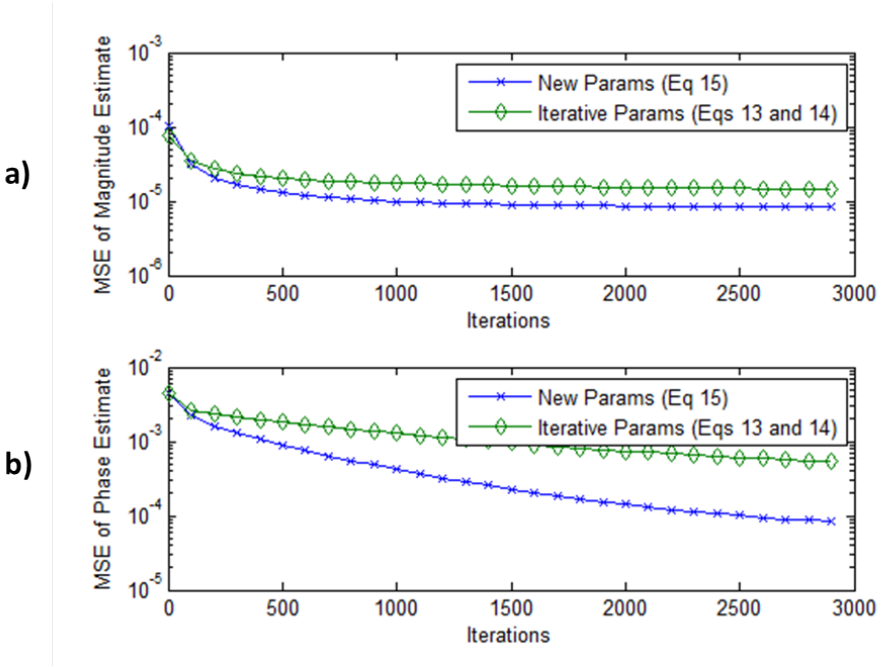

Figure 50. Error curves for Figure 49 showing MSE computed between estimated and true object function: a) magnitude and b) phase.

5.3 Expanding Algorithm to Experimental Data

Introduction of bias retardation to the DIC system previously relied on two suboptimal approaches. The first is introducing a quarter wave plate and rotating the analyzer.[2] The second involves laterally shifting the objective Nomarski prism through the imaging path. Neither of these approaches produces accurate, repeatable results nor is it possible to easily determine the bias introduced in this manner. Another parameter, the shear distance, is also difficult to quantify using traditional Nomarski DIC hardware. Methods utilizing images of sub-resolution samples have been applied with limited success, but have drawbacks that make them undesirable when accuracy is paramount. The development of techniques using liquid crystal devices has helped overcome these

hurdles. It is now possible to finely control the bias retardation used when imaging a sample and to apply the same bias to future experiments. These devices also enabled the accurate measuring the shear distance.

The use of new data processing techniques has also contributed to the quality of estimations possible with this algorithm. A method for registering rotationally diverse DIC images using phase correlation of bright field images was explored. The effects of misregistration are significant on the final outcome of the AM algorithm as shown in Figure 33. The experimental bead data in Figure 39c shows this to be true even on a simple object with virtually no features. Other artifacts, as seen in Figure 41, are manifestations of the ill-posed nature of the system. The use of a roughness penalty in the AMA, as well as removing the background shift in the image, helps to mitigate some of these effects as demonstrated in Figure 43. The outcome of this AM algorithm on experimental data has been validated through the use of simulated approximations of the experimental data as well as processing of the data using a secondary quantitative phase imaging algorithm.

5.4 Future Work

Further expansion of this work would be best focused on improving the determination of model parameter, α, β, and γ, related to minimizing the objective function. These have continually proven to be a source of problems. As the algorithm has grown in complexity the determination of these parameters has grown right along with it. Originally developed to be simple analytical quantities based upon the convolution kernel derived from the PSF, they quickly turned into an iterative minimization algorithm of their own (Eqs. (13) and (14)). Computation of parameters

using these equations proved problematic and extremely costly even for the smallest datasets. Rough approximations were derived to mitigate some of the issue in using them, but this required too many adjustable parameters. While most any values calculated using the approximation will function, they converge to unacceptably attenuated and smoothed results. The development of the parameter model defined in Eq. (15) was a major turning point in this thesis without which most of the results shown would not have been possible.

A second body of work that is in need of investigation is the implementation of the algorithm itself. Much of the original research into this approach to quantitative phase imaging was focused on the convergence properties of the algorithm. This was accomplished by representing the system in linear algebra form with the PSF converted into a convolution kernel. Rather than convolving an NxN image with an NxN PSF, instead an N^2xN^2 matrix and an Nx1 vector are multiplied. This results in an algorithm with exponentially growing memory and computational cost. Now that this particular implementation requirement no longer exists, and the algorithms efficacy has been validated, a rewriting of the codebase to a more sensible implementation is advisable.

Lastly, the registration of the rotationally diverse data can use improvement. The SPI algorithm utilizes the phase shifted images for a given shear to determine a phase gradient for that shear direction. This gradient is easier to use in registration than the raw DIC images. AMA's current utilization of bright field images for the registration step aims to achieve the same end result. Unfortunately the bright field images have low signal content due to the weak absorption properties of the sample. This poses a challenge for the phase correlation as the noise patterns are dominant over the portions of

the image of interest. The use of image segmentation approaches, thresholding, and boundary detection are all possible candidates for either augmenting or replacing phase correlation for image registration.

REFERENCES

[1] M.R. Arnison, K. G. Larkin, C. J. Sheppard, N. I. Smith, and C. J. Cogswell, "Linear phase imaging using differential interference contrast microscopy," *J.Microsc.* **214**(1), 7-12 (2004).

[2] S. V. King, *Quantitative Phase Information from Differential Interference Contrast Microscopy*, Ph.D. Dissertation, University of Colorado at Boulder, (2009).

[3] C. Preza, *Phase Estimation using Rotational Diversity for Differential Interference Contrast Microscopy*, Ph.D. Dissertation, Washington University, (1998).

[4] J. A. O'Sullivan and C. Preza, "Alternating minimization algorithm for quantitative differential-interference contrast (DIC) microscopy," *Electronic Imaging 2008*, 68140Y-68140Y-11 (2008).

[5] J. A. O'Sullivan and C. Preza, "Quantitative determination of specimen properties using computational differential-interference contrast (DIC) microscopy," *European Conference on Biomedical Optics*, 6630_13 (2007).

[6] J. A. O'Sullivan and C. Preza, "Computational Differential Interference Contrast (DIC) Microscopy for Quantitative Imaging," *Computational Optical Sensing and Imaging*, CThB5 (2009).

[7] J. A. O'Sullivan and C. Preza, "Quantitative phase and amplitude imaging using differential-interference contrast (DIC) microscopy," *IS&T/SPIE Electronic Imaging*, 724604-724604-11 (2009).

[8] J. A. O'Sullivan and C. Preza, "Implementation and evaluation of a penalized alternating minimization algorithm for computational DIC microscopy," *IS&T/SPIE Electronic Imaging*, 75330E-75330E-11 (2010).

[9] H. Sierra, C. DiMarzio, and D. Brooks, "Modeling dic microscope images of thick objects using a product-of-convolutions approach," *Biomedical Optics*, BMD67 (2008).

[10] H. Sierra, C. DiMarzio, and D. Brooks, "Modeling images of phase information for three-dimensional objects," *Biomedical Optics (BiOS)* 2008, 68610A-68610A-9 (2008).

[11] H. Sierra, C. DiMarzio, and D. Brooks, "Modeling phase microscopy of transparent three-dimensional objects: a product-of-convolutions approach," *JOSA A* **26**(5), 1268-1276 (2009).

[12] H. Sierra, C. DiMarzio, and D. Brooks, "3D reconstruction for multimodality phase microscopy using boundary detection constraints," *Biomedical Imaging: From Nano to Macro, 2010 IEEE International Symposium on*, 1125-1128 (2010).

[13] M. Shribak and S. Inoué, "Orientation-independent differential interference contrast microscopy," *Appl. Opt.* **45**(3), 460-469 (2006).

[14] M. Shribak, J. LaFountain, D. Biggs and S. Inoué, "Orientation-independent differential interference contrast microscopy and its combination with an orientation-independent polarization system," *J. Biomed. Opt.* **13**(1), 014011-014011-10 (2008).

[15] M. Shribak, J. LaFountain, D. Biggs, and S. Inoué, "Quantitative orientation-independent differential interference contrast (DIC) microscopy," *Biomedical Optics (BiOS)* 2007, 64411L-64411L-12 (2007).

[16] J. A. O'Sullivan and J. Benac, "Alternating minimization algorithms for transmission tomography," *Medical Imaging, IEEE Transactions on* **26**(3), 283-297 (2007).

[17] Y. Wang, J. Yang, W. Yin, and Y. Zhang, "A new alternating minimization algorithm for total variation image reconstruction," *SIAM Journal on Imaging Sciences* **1**(3), 248-272 (2008).

[18] W. Byrne, "Alternating minimization and Boltzmann machine learning," *Neural Networks, IEEE Transactions on*, **3**(4), 612-620 (1992).

[19] J. Wang, T. Jebara, and S. Chang, "Graph transduction via alternating minimization," *Proceedings of the 25th International Conference on Machine Learning*, 1144-1151 (2008).

[20] A. Gunawardana and W. Byrne, "Convergence theorems for generalized alternating minimization procedures," *The Journal of Machine Learning Research* **6**, 2049-2073 (2005).

[21] R. D. Guenther, *Modern Optics*, Wiley, New York (1990).

[22] C. J. Cogswell and C. Sheppard, "Confocal differential interference contrast (DIC) microscopy: including a theoretical analysis of conventional and confocal DIC imaging," *J. Microsc.* **165**(1), 81-101 (1992).

[23] M. Born and E. Wolf, *Principles of Optics: Electromagnetic Theory of Propagation, Interference and Diffraction of Light*, CUP Archive (1999).

[24] C. Preza, D. L. Snyder, and J. Conchello, "Theoretical development and experimental evaluation of imaging models for differential-interference-contrast microscopy," *JOSA A* **16**(9), 2185-2199 (1999).

[25] D. A. Boas, C. Pitris, and N. Ramanujam, *Handbook of Biomedical Optics*, CRC Press (2012).

[26] S. P. Boyd and L. Vandenberghe, *Convex Optimization*, Cambridge University Press, New York (2004).

[27] E. Van Munster, L. Van Vliet, and J. Aten, "Reconstruction of optical pathlength distributions from images obtained by a wide-field differential interference contrast microscope," *J.Microsc.* **188**(2), 149-157 (1997).

[28] S. B. Mehta and C. J. Sheppard, "Sample-less calibration of the differential interference contrast microscope," *Appl.Opt.* **49**(15), 2954-2968 (2010).

[29] V. Munster, "Measurement-based evaluation of optical pathlength distributions reconstructed from simulated differential interference contrast images," *J.Microsc.* **191**(2), 170-176 (1998).